REPORT DOCUMENTATION PAGE

Form Approved OMB NO. 0704-0188

1. REPORT DATE (DD-MM-YYYY)	2. REPORT TYPE	3. DATES COVERED (From - To)
11-08-2016	Final Report	20-Aug-2012 - 19-Aug-2016

4. TITLE AND SUBTITLE
Final Report: Strain-Induced Phase Transformations in Ceramics under High Pressure

5a. CONTRACT NUMBER
W911NF-12-1-0340

5b. GRANT NUMBER

5c. PROGRAM ELEMENT NUMBER
611102

6. AUTHORS
Valery Levitas, Yanzhang Ma

5d. PROJECT NUMBER

5e. TASK NUMBER

5f. WORK UNIT NUMBER

7. PERFORMING ORGANIZATION NAMES AND ADDRESSES
Iowa State University of Science and Techn
1138 Pearson Hall
505 Morrill Road
Ames, IA 50011 -2103

8. PERFORMING ORGANIZATION REPORT NUMBER

9. SPONSORING/MONITORING AGENCY NAME(S) AND ADDRESS (ES)
U.S. Army Research Office
P.O. Box 12211
Research Triangle Park, NC 27709-2211

10. SPONSOR/MONITOR'S ACRONYM(S)
ARO

11. SPONSOR/MONITOR'S REPORT NUMBER(S)
61707-MS.40

12. DISTRIBUTION AVAILIBILITY STATEMENT
Approved for Public Release; Distribution Unlimited

13. SUPPLEMENTARY NOTES
The views, opinions and/or findings contained in this report are those of the author(s) and should not contrued as an official Department of the Army position, policy or decision, unless so designated by other documentation.

14. ABSTRACT
The objectives included theoretical, computational, and experimental investigations of phase transformations (PTs) in ceramics under high pressure and large plastic shear. Main results:
-Algorithm for contact sliding between diamond, gasket, and sample is developed. Strain-induced PTs under compression, compression and torsion, unloading, and reloading in a rotational diamond anvil cell (RDAC) are studied in detail. Various experimental phenomena are reproduced. Possible misinterpretations of experiments are demonstrated. Ways to extract kinetic information from heterogeneous experimental fields are suggested.

15. SUBJECT TERMS
phase transformations under compression and shear, ceramics, boron nitride, rotational diamond anvil cell, finite element modeling, phase field approach.

16. SECURITY CLASSIFICATION OF:			17. LIMITATION OF ABSTRACT	15. NUMBER OF PAGES	19a. NAME OF RESPONSIBLE PERSON
a. REPORT	b. ABSTRACT	c. THIS PAGE			Valery Levitas
UU	UU	UU	UU		19b. TELEPHONE NUMBER 515-294-9691

Report Title

Final Report: Strain-Induced Phase Transformations in Ceramics under High Pressure

ABSTRACT

The objectives included theoretical, computational, and experimental investigations of phase transformations (PTs) in ceramics under high pressure and large plastic shear. Main results:

-Algorithm for contact sliding between diamond, gasket, and sample is developed. Strain-induced PTs under compression, compression and torsion, unloading, and reloading in a rotational diamond anvil cell (RDAC) are studied in detail. Various experimental phenomena are reproduced. Possible misinterpretations of experiments are demonstrated. Ways to extract kinetic information from heterogeneous experimental fields are suggested.

-New mechanism of plastic deformation and stress relaxation at high strain-rates (10^9-10^12 s^-1) via virtual melting 4000 K below the melting temperature is predicted using new thermodynamic theory and confirmed by molecular dynamic simulations.

-PT from disordered nanocrystalline hexagonal (h)BN to superhard wurtzitic (w)BN was found at 6.7 GPa under plastic shear in RDAC. Under hydrostatic compression to 52.8GPa, hBN did not transform.

-Developments in the phase field approach:

a)General theory for multivariant martensitic PTs (including interface stresses and anisotropic interface energy), dislocations, & interaction of dislocations and PTs and explicit models are formulated at large strains.

b)Finite-element approach is developed and numerous problems are solved, including interaction between PT and plasticity under compression and shear in nanograin material.

Enter List of papers submitted or published that acknowledge ARO support from the start of the project to the date of this printing. List the papers, including journal references, in the following categories:

(a) Papers published in peer-reviewed journals (N/A for none)

Received	Paper

TOTAL:

Number of Papers published in peer-reviewed journals:

(b) Papers published in non-peer-reviewed journals (N/A for none)

Received	Paper

TOTAL:

Number of Papers published in non peer-reviewed journals:

(c) Presentations

1. V. I. Levitas. Effect of two nanoscale size parameters on the macroscopic transformation behavior within phase field approach. 52nd Annual Meeting Society of Engineering Science, College Station, TX, 10/25/15-10/28/15.
2. B. Feng and V. I. Levitas. Large deformation model with coupled plasticity and strain-induced phase transformation in a diamond anvil cell. 52nd Annual Meeting Society of Engineering Science, College Station, TX, 10/25/15-10/28/15.
3. K. Momeni and V. I. Levitas. Phase-Field Approach to Nonequilibrium Phase Transformation with Moving Interfacial Phases and Interfacial Tension. 52nd Annual Meeting Society of Engineering Science, College Station, TX, 10/25/15-10/28/15.
4. A. Roy and V. I. Levitas. Generalized multiphase phase field theory for temperature- and stress-induced phase transformation. 52nd Annual Meeting Society of Engineering Science, College Station, TX, 10/25/15-10/28/15.
5. Y. S. Hwang and V. I. Levitas. Coupled phase field, heat conduction, and elastodynamic simulation of kinetic superheating and melting of aluminum nanolayer irradiated by picosecond laser. 52nd Annual Meeting Society of Engineering Science, College Station, TX, 10/25/15-10/28/15.
6. Levitas, V. New multiphase phase field approach for temperature- and stress-induced phase transformations. NIST, Gaithersburg, MD, December 12, 2015.
7. V. I. Levitas. Phase field approach to interface- and surface-induced phenomena. Plasticity'16 International Symposium, Kona, Hawaii (Keynote lecture), 3/1/16-9/1/16
8. V. I. Levitas. Interaction between Phase Transformation and Plasticity. International conference on Emerging Trends In Applied Mathematics And Mechanics, Perpignan, France, May 28-June 2, 2016, Keynote lecture.
9. V. I. Levitas. Multiphase phase field theory for phase transformation. European Congress on Computational Methods in Applied Sciences and Engineering, Crete Island, Greece, 5/6/16-10/6/16.
10. V. I. Levitas. Phase field approach to structural changes. United Technology Research Center, East Hartford, CN, April 5, 2016.

Number of Presentations: 10.00

Non Peer-Reviewed Conference Proceeding publications (other than abstracts):

Received	Paper

TOTAL:

Number of Non Peer-Reviewed Conference Proceeding publications (other than abstracts):

Peer-Reviewed Conference Proceeding publications (other than abstracts):

Received	Paper

TOTAL:

Number of Peer-Reviewed Conference Proceeding publications (other than abstracts):

(d) Manuscripts

Received Paper

TOTAL:

Number of Manuscripts:

Books

Received Book

TOTAL:

Received Book Chapter

TOTAL:

Patents Submitted

Patents Awarded

Awards

PI's Honors

- Alexander von Humboldt Foundation Fellowship for alumni for 3 months research in Germany, including support for post doc from the USA
- Who's Who in America, 2012, 2013, 2014 and 2015, 2016
- Who's Who in the World, 2012, 2013, 2014 and 2015, 2016
- Dictionary of International Biography, 2012, 2014
- 2000 Outstanding Intellectuals of the 21st Century, 2014
- Who's Who in Science and Engineering, 2016

ISU Award for Outstanding Achievement in Research for 2016

Student Awards

Biao Feng, PhD student, currently post doc at ISU:
Iowa State University Research Excellence Award for Fall 2014; 2015 Alexander Lippisch Memorial Scholarship.

Kasra, Momeni, PhD student, currently post doc at Penn State: Iowa State University Teaching Excellence Award for Fall 2014;
Research Award from Graduate and Professional Student Senate of ISU, Spring 2015; Teaching Award from Graduate and Professional Student Senate of ISU, 2015;
Iowa State University Research Excellence Award for Summer 2015.
2016 Zaffarano Prize Honorable Mention for excellent graduate research at ISU.

Mahdi Javanbakht, PhD student and post doc:
Karas Award for Outstanding Dissertation in the Mathematical and Physical Sciences, and Engineering discipline at Iowa State University, 2014.

Graduate Students

NAME	PERCENT_SUPPORTED	Discipline
Yang Gao	0.50	
Lin Lin	0.20	
Hamed Babaei	0.30	
FTE Equivalent:	**1.00**	
Total Number:	**3**	

Names of Post Doctorates

NAME	PERCENT_SUPPORTED
Haiyan Wang	0.50
Weihong Xue	0.10
Jianguo Du	0.10
Biao Feng	0.50
Arunabha Roy	0.25
Kasra Momeni	0.20
Mahdi Javanbakht	0.00
FTE Equivalent:	**1.65**
Total Number:	**7**

Names of Faculty Supported

NAME	PERCENT_SUPPORTED	National Academy Member
Valery Levitas	0.33	
Yanzhang Ma	0.10	
FTE Equivalent:	**0.43**	
Total Number:	**2**	

Names of Under Graduate students supported

NAME	PERCENT_SUPPORTED
FTE Equivalent:	
Total Number:	

Student Metrics

This section only applies to graduating undergraduates supported by this agreement in this reporting period

The number of undergraduates funded by this agreement who graduated during this period:	0.00
The number of undergraduates funded by this agreement who graduated during this period with a degree in science, mathematics, engineering, or technology fields:.....	0.00
The number of undergraduates funded by your agreement who graduated during this period and will continue to pursue a graduate or Ph.D. degree in science, mathematics, engineering, or technology fields:.....	0.00
Number of graduating undergraduates who achieved a 3.5 GPA to 4.0 (4.0 max scale):.....	1.00
Number of graduating undergraduates funded by a DoD funded Center of Excellence grant for Education, Research and Engineering:.....	0.00
The number of undergraduates funded by your agreement who graduated during this period and intend to work for the Department of Defense	0.00
The number of undergraduates funded by your agreement who graduated during this period and will receive scholarships or fellowships for further studies in science, mathematics, engineering or technology fields:	0.00

Names of Personnel receiving masters degrees

NAME
Total Number:

Names of personnel receiving PHDs

NAME
Total Number:

Names of other research staff

NAME	PERCENT_SUPPORTED
FTE Equivalent:	
Total Number:	

Sub Contractors (DD882)

Inventions (DD882)

Scientific Progress

See Attachment

Technology Transfer

V. I. Levitas gave the following talk and had discussions at ARL and ARO sponsored meetings:
1. V. I. Levitas. Pressure and shear induced phase transformations in ceramics (invited lecture). 37th International Conference and
Exposition on Advanced Ceramics and Composites, Armor Ceramics Symposium, Daytona Beach, Florida, January 27-February 2, 2013.
2. V. I. Levitas. Phase field approach to dynamics of phase transformations and plasticity at nano and microscales. 04/09/2013, ARL,
Aberdeen, MD.
3. V. I. Levitas. Phase field approach to structural changes at the nanoscale. Mach Conference, Annapolis, MD, 04/09/2013-04/12/2013.
4. V. I. Levitas. Strain-Induced Phase Transformations under High Pressure: Three-Scale Theory and Simulations and Interpretation of
Experiments. Mach Conference, Annapolis, MD, 04/09/2013-04/12/2013.
5. Goddard W.A., Levitas V.I., Ma Y. New Pathways toward Metastable Solids through Moderate Pressure and Large Plastic Shear: Multiscale Simulations and Experiments. DARPA Extended Solids Grantee Meeting, Arlington, VA, 9/23/13-9/24/13.
6. Levitas V.I. Phase field approach to phase transformations, plasticity, and interface phenomena. John Hopkins University, Hopkins Extreme Materials Institute, Baltimore, MD, 11/15/2013.
7. V. I. Levitas. Phase transformations under high pressure and large plastic shear. Materials in Extreme Environments, Army Science Planning and Strategy Meeting, Towson, MD, 12/10/13-12/11/13 (invited talk).
8. V. I. Levitas. Evolving interfaces: phase field approach. Mach Conference, Annapolis, MD, 04/09/2014-04/11/2014.
9. V. I. Levitas. Phase Transformations under High Pressure and Large Plastic Shear in Rotational Diamond Anvils. Mach Conference, Annapolis, MD, 04/09/2014-04/11/2014.

V. I. Levitas gave the following talk and had discussions at Geophysical Laboratory, Carnegie Institution of Washington:
1. V. I. Levitas. Ways of characterization of pressure-, stress-, and strain-induced phase transformations. Invited Seminar at Geophysical Laboratory, Carnegie Institution of Washington, December, 13, 2014.
2. V. I. Levitas. Phase transformations under high pressure and large plastic shear, Invited Seminar at Geophysical Laboratory, Carnegie Institution of Washington, April 7, 2014.
3. V. I. Levitas. Strain-induced versus pressure-induced phase transformations under high pressure, Invited Seminar at Geophysical Laboratory, Carnegie Institution of Washington, September 10, 2014.
4. V. I. Levitas. New multiphase phase field approach for temperature- and stress-induced
phase transformations. NIST, Gaithersburg, MD, December 12, 2015.
5. V. I. Levitas. Phase field approach to structural changes. United Technology Research Center, East Hartford, CN, April 5, 2016.

(4) Scientific Progress and Accomplishments

1. Theoretical and Computational Studies

1.1. Strain-induced phase transformations under compression, unloading, and reloading in a diamond anvil cell [7]

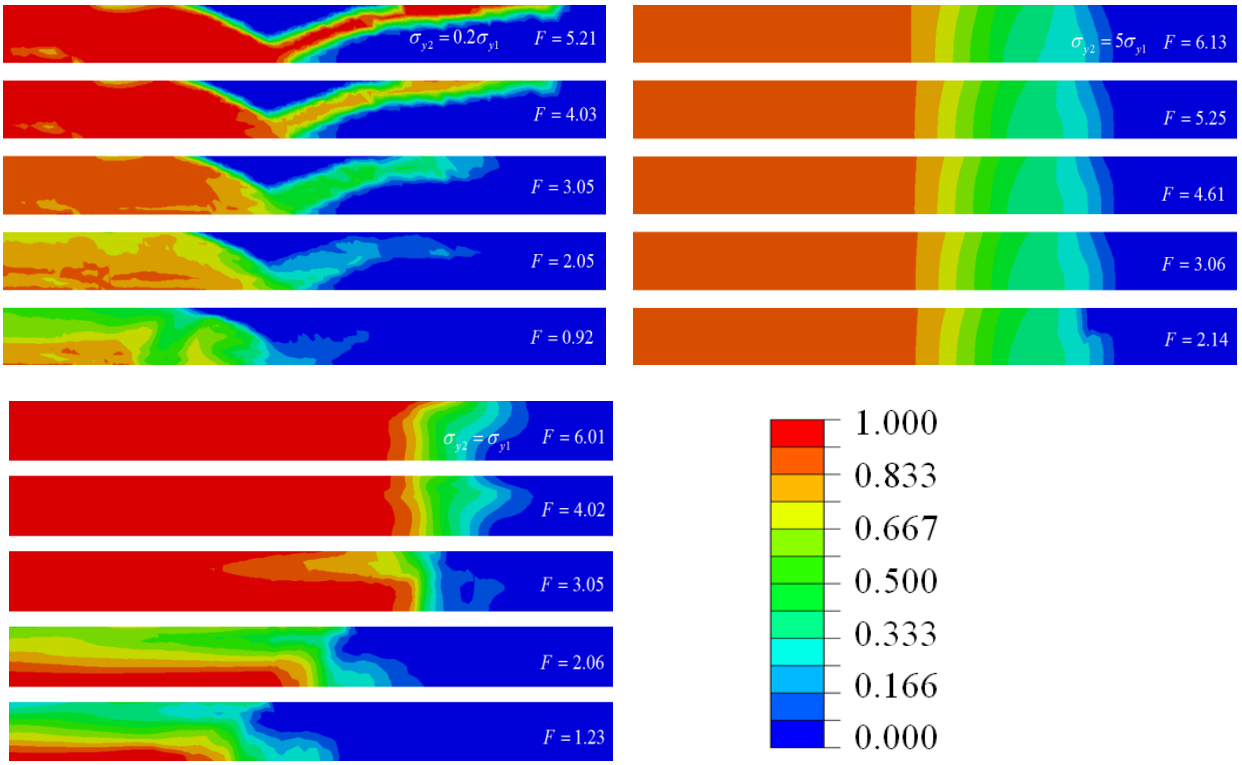

Fig. 1. Concentration of high pressure phase c in the sample after compression under unloading for fast kinetics ($k = 30$) and three different ratios of the low and high pressure phases ($\sigma_{y2} = 0.2\sigma_{y1}$, $\sigma_{y2} = \sigma_{y1}$, and $\sigma_{y2} = 5\sigma_{y1}$). For weaker and equal-strength high pressure phase, significant plastic flow and reverse phase transformation occurs under unloading, which may lead to significant misinterpretation of experiments for recovered sample. For high strength high pressure phase, plastic flow and reverse strain-induced phase transformation under unloading is negligible.

Strain-induced phase transformations (PTs) in a sample under compression, unloading, and reloading in a diamond anvil cell (DAC) are investigated in detail, by applying finite element method. In contrast to previous studies, the kinetic equation includes the pressure range, in which both direct and reverse PTs occur simultaneously. Results are compared to the case when "no transformation" region in the pressure range exists instead, for various values of the kinetic parameters and ratios of the yield strengths of low and high pressure phases. Under unloading (which has never been studied before), surprising plastic flow and reverse PT are found, which were neglected in experiments and change interpretation of experimental results. They are caused both by heterogeneous stress redistribution and transformation-induced plasticity. After reloading, the reverse PT continues followed by intense direct PT. However, PT is less

pronounced than after initial compression and geometry of transformed zone changes. In particular, a localized transformed band of a weaker high pressure phase does not reappear in comparison with the initial compression. A number of experimental phenomena are reproduced and interpreted.

1.2. Plastic flows and phase transformations in materials under compression in diamond anvil cell: Effect of contact sliding [1]

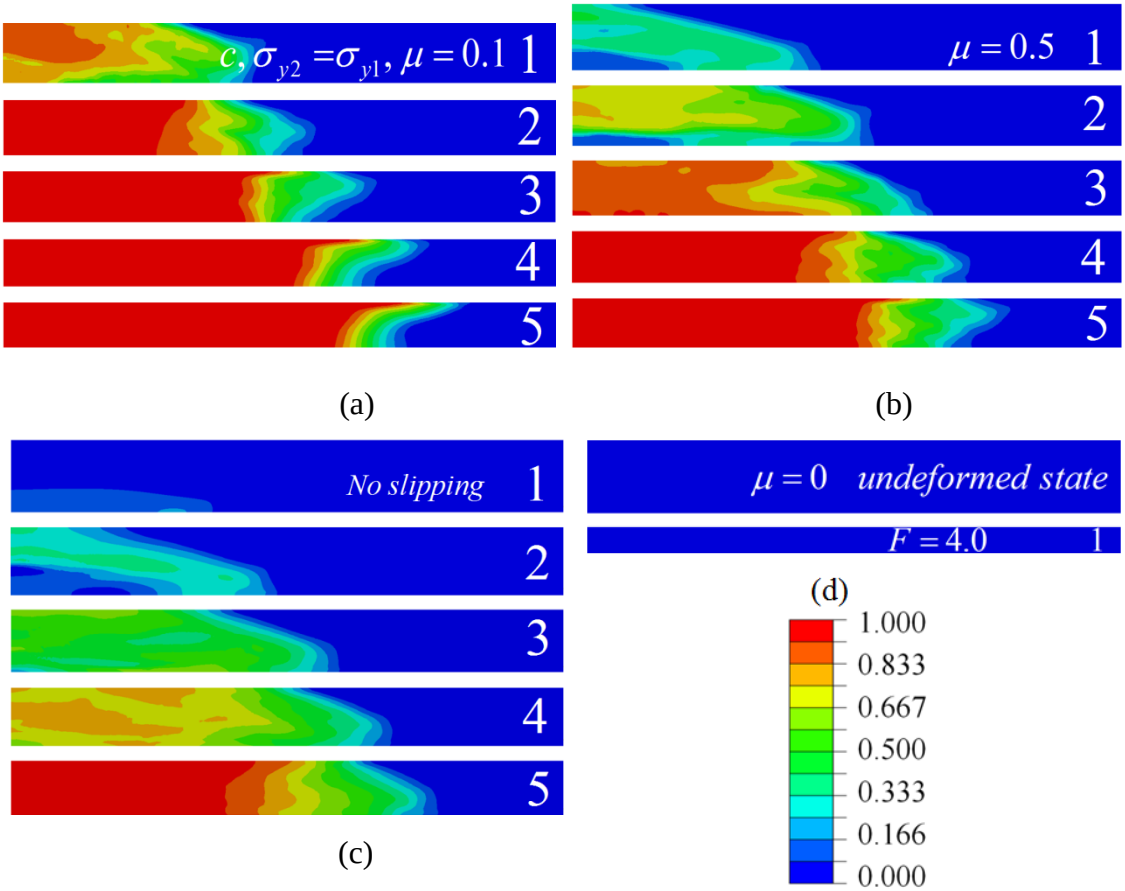

Fig. 2. Distribution of high-pressure phase concentration c, for $k = 30$, equal strength phases $\sigma_{y2} = \sigma_{y1}$, and coefficient of friction (a) $\mu = 0.1$, (b) $\mu = 0.5$ and (d) $\mu = 0$, and (c) no slipping model.

Modeling of coupled plastic flows and strain-induced phase transformations under high pressure in a DAC is performed with the focus on the effect of the contact sliding between sample and anvils. Equations for a combination of Coulomb friction and plastic friction with variable parameters due to PT are formulated and corresponding computational algorithm is developed. Finite element software ABAQUS is utilized. Results are obtained for PTs to weaker, equal-strength, and stronger high pressure phases, using different scaling parameters in a strain-controlled kinetic equation, and with various friction coefficients. Compared to the model with cohesion, artificial shear banding near the constant surface is eliminated. Sliding and the reduction in friction coefficient intensify radial plastic flow in the entire sample (excluding a narrow region near the contact surface) and a reduction in thickness. A reduction in the friction

coefficient to 0.1 intensifies sliding and increases pressure in the central region. Increases in both plastic strain and pressure lead to intensification of strain-induced PT. The effect of self-locking of sliding is revealed. Multiple experimental phenomena are reproduced and interpreted. Thus, plastic flow and PT can be controlled by controlling friction.

1.3 Strain-induced phase transformations and plastic flows under high pressure and torsion in a rotational diamond anvil cell: Simulation of loading, unloading, and reloading [13]

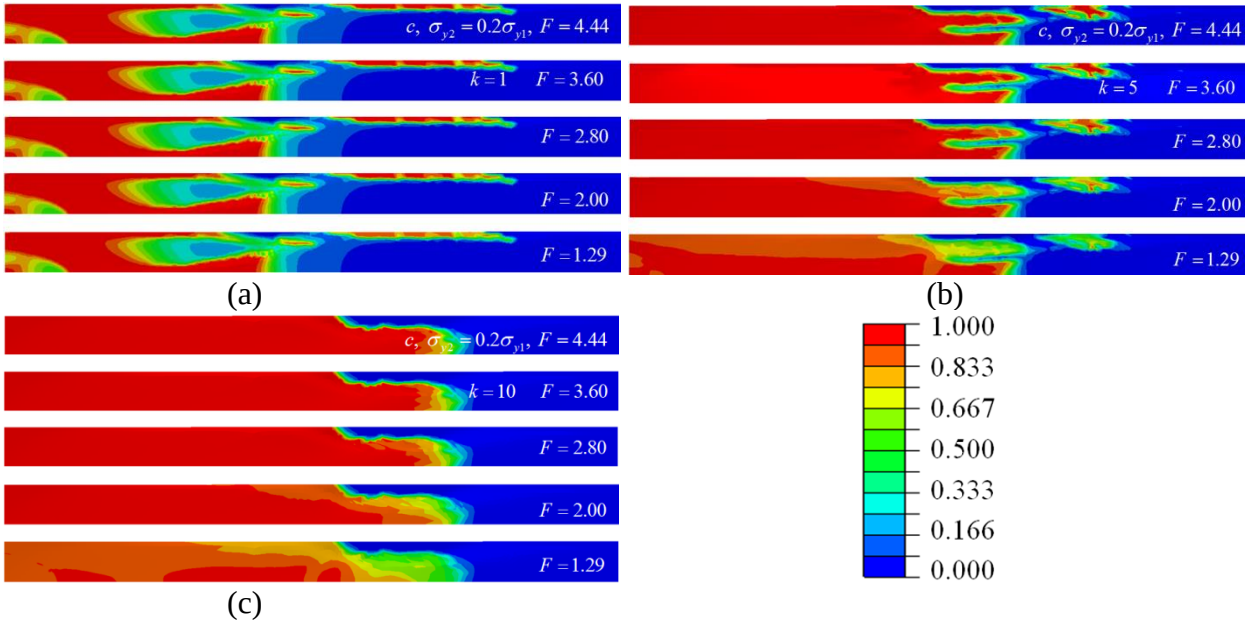

Fig.3. Concentration of high-pressure phase c with decreasing axial compressive force F under a constant rotation angle 0.84, for $\sigma_{y2} = 0.2\sigma_{y1}$, and k=1, 5 and 10.

Coupled plastic flow and strain-induced PTs under high pressure and torsion in a micron scale sample under loading, unloading, and reloading in a rotational diamond anvil cell (RDAC) are studied in detail, utilizing finite element approach. A plastic strain-controlled, pressure-dependent kinetic equation, which describes strain-induced PTs, is used. The effects of four main material parameters in this equation on PTs and plastic flow in RDAC in three-dimensional formulation are systematically analyzed. Multiple experimental phenomena are reproduced and interpreted, including pressure self-multiplication/demultiplication effects, small 'steps' on pressure distribution in the two-phase region, simultaneous occurrences of direct and reverse PTs, oscillatory distribution of pressure for weaker high-pressure phase, and a thin layer of high-pressure phase on a contact surface. During unloading, unexpected intensive plastic flow and reverse PT are revealed, which change the interpretation of experimental results. The effect of unloading and reloading paths on PTs is examined. Two types of pressure variations are revealed, which are qualitatively consistent within experimental observations for ZnSe and KCl. Obtained results lead to ways of controlling PTs by varying compression-torsion paths and can be utilized for the search of new high pressure phases, ways to reduce pressure for the synthesis of high pressure phases, and to retain them at ambient pressure.

1.4 Strain-induced phase transformations under high pressure and large shear in a rotational diamond anvil cell: Effect of contact sliding [11]

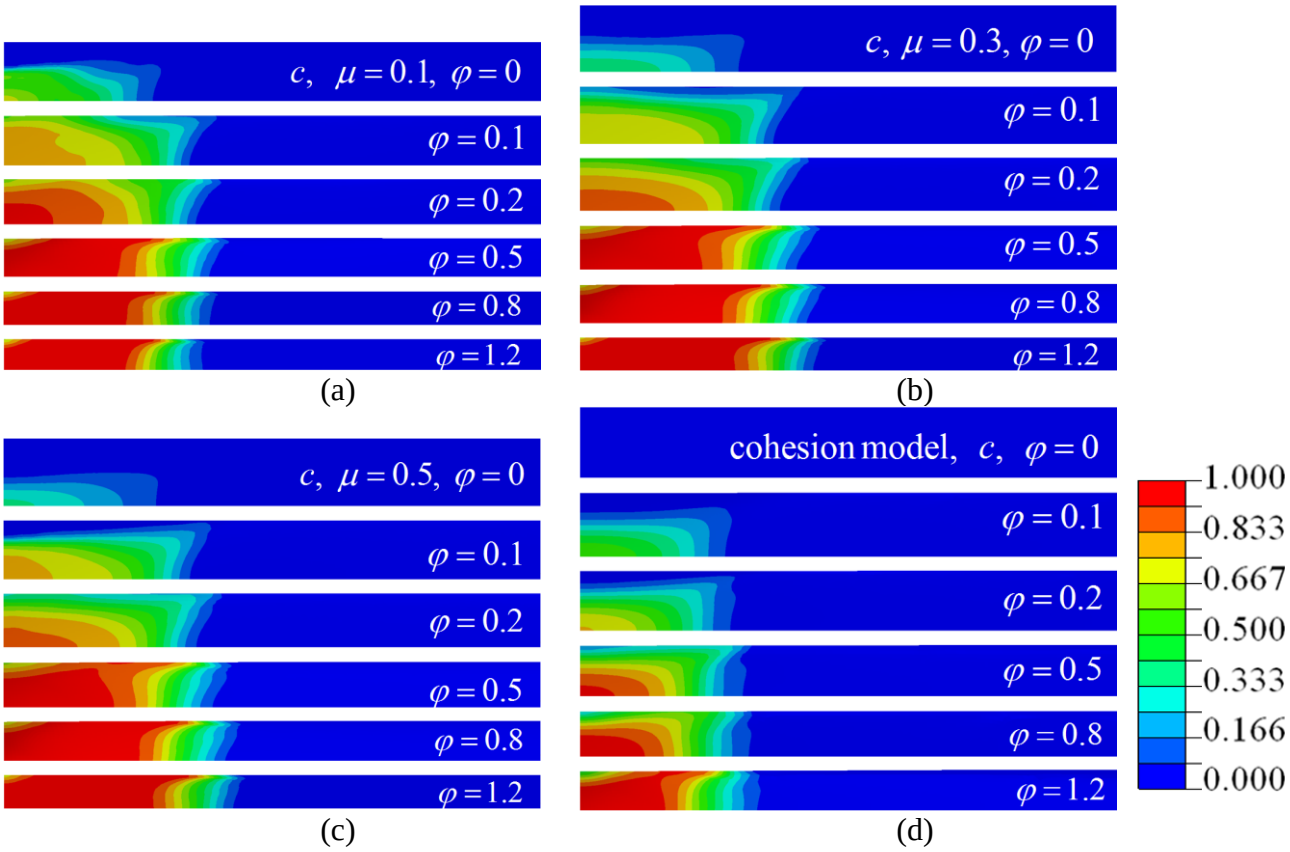

Fig. 4. Change in concentration of high-pressure phase c with growing rotation angle φ under a constant compressive axial force F=3.75, for k=5, $\sigma_{y2} = \sigma_{y1}$ and $r/R \le 0.72$. Rotation angle is (1) 0, (2) 0.1, (3) 0.2, (4) 0.5, (5) 0.8, (6) 1.2. (a), (b) and (c) are for the contact model with friction coefficients of 0.1, 0.3 and 0.5, respectively; (d) is for cohesion model.

A three-dimensional large-sliding contact model coupled with strain-induced PTs and plastic flow in a disk-like sample under torsion at high pressure in RDAC is formulated and studied. Coulomb and plastic friction are combined and variable parameters due to PT are taken into account. Results are obtained for weaker, equal-strength, and stronger high pressure phases, and for three values of the kinetic coefficient in a strain-controlled kinetic equation and friction coefficient. All drawbacks typical of problem with cohesion are overcome, including eliminating mesh-dependent shear band and artificial plastic zones. Contact sliding intensifies radial plastic flow, which leads to larger reduction in sample thickness. Larger plastic strain and increased pressure in the central region lead to intensification of PT. However, the effect of the reduction in the friction coefficient on PT kinetics is nonmonotonous. Sliding increases away from the center and with growing rotation, and is weakly dependent on the kinetic coefficient. Also, cyclic back and forth torsion is studied and compared to unidirectional torsion. Multiple experimental phenomena, e.g., pressure self-multiplication effect, steps (plateaus) at pressure distribution, flow to the center of a sample, and oscillatory pressure distribution for weaker high-pressure phase, are reproduced and interpreted. Reverse PT in high pressure phase that flowed to the low

pressure region is revealed. Possible misinterpretation of experimental PT pressure is found. Obtained results represent essential progress toward understanding of strain-induced PTs under compression and shear in RDAC and may be used for designing experiments for synthesis of new high pressure phases and reduction in PT pressure for known phases, as well as for determination of PT kinetics from experiments.

1.5 Strain-induced phase transformation under compression in a diamond anvil cell: simulations of a sample and gasket [14]

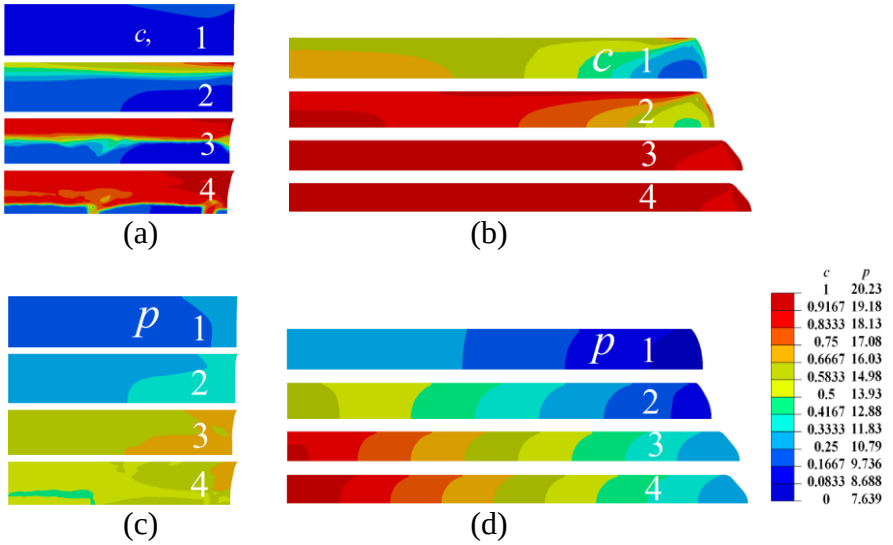

Fig. 5. Distributions of concentration of high-pressure phase *c*, and pressure *p* in the sample for $H_1 = H_0$ and $\sigma_{yg} = 3\sigma_{y1}$, for relative sample radii $S = 0.4$ ((a) and (c)) and $S = 0.7$ ((b) and (d)). The dimensionless axial force *F* is (1) 8.19, (2) 9.22, (3) 10.85, (4) 11.13.

Combined high pressure PTs and plastic flow in a sample within a gasket compressed in DAC are studied for the first time using finite element method (FEM). The key point is that phase transformations are modelled as strain-induced, which involves a completely different kinetic description than for traditional pressure-induced PTs. The model takes into account contact sliding with Coulomb and plastic friction at the boundaries between the sample, gasket and anvil. A comprehensive computational study of the effects of the kinetic parameter, ratio of the yield strengths of high and low-pressure phases and the gasket, sample radius and initial thickness on the PTs and plastic flow is performed. A new sliding mechanism at the contact line between the sample, gasket, and anvil called extrusion-based pseudoslip is revealed, which plays an important part in producing high pressure. Strain-controlled kinetics explains why experimentally determined phase transformation pressure and kinetics (concentration of high pressure phase vs. pressure) differ for different geometries and properties of the gasket and the sample: they provide different plastic strain, which was not measured. Utilization of the gasket changes radial plastic flow toward the center of a sample, which leads to high quasi-homogeneous pressure for some geometries. For transformation to a stronger high pressure phase, plastic strain and concentration of a high-pressure phase are also quasi-homogeneous. This allowed us to suggest a method of determining strain-controlled kinetics from experimentation, which is not possible for weaker and equal-strength high-pressure phases and

cases without a gasket. Some experimental phenomena are reproduced and interpreted. Developed methods and obtained results represent essential progress toward the understanding of PTs under compression in the DAC. This will allow one optimal design of experiments and conditions for synthesis of new high pressure phases.

1.6. Virtual Melting: A New Mechanism of Stress Relaxation under High Strain Rate Loading [10]

We revealed a new and unexpected mechanism of plastic deformation and stress relaxation at high strain-rates (10^9-10^{12} s^{-1}). Namely, work and energy of nonhydrostatic stresses cause a crystal to undergo melting much *(4000 K!)* below the melting temperature at the corresponding hydrostatic pressure. After melting, the stress relaxation leads to an undercooled liquid, which recrystallizes within picosecond time scales. Such a virtual melting is predicted using a newly developed thermodynamic approach for melting under shock loading and high strain rates. We have confirmed this mechanism of virtual melting via large-scale molecular dynamics simulations in Cu and Al with embedded atom method (EAM) interatomic potentials and also in Lennard-Jones systems. Since thermodynamic consideration is quite generic, this mechanism is expected in many other materials.

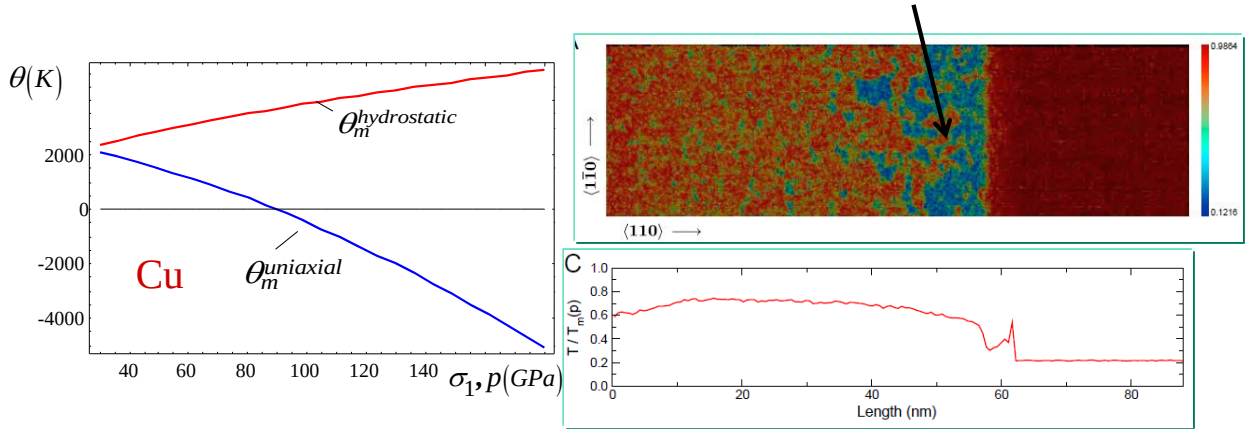

Fig. 6. (left) Calculated melting temperature under hydrostatic and uniaxial conditions vs. pressure (uniaxial load) for shock loading of Cu along the <110> direction;

(right). Atomic configuration of Cu slab shocked to a pressure of 160 GPa (red atoms are solid, blue are liquid) and temperature profiles along shock direction. The temperature is normalized by the equilibrium melt temperature T_m (p) at the corresponding shock pressure along the profile.

This is a new and much unexpected result, which changes our understanding of melting phenomena in general and significantly advances general continuum thermodynamics under nonhydrostatic loading. Our results may also impact the interpretation of current and future experiments in shock-wave physics at ultrahigh pressures and add a new mechanism to the deformation-mechanism maps. The strain rates regime explored in this work is relevant to planned experiments in large laser facilities such as the National Ignition Facilities at Lawrence

Livermore National Laboratory in the United States and LULI (Laboratoire pour l'Utilisation des Lasers Intenses) in France. They are also relevant for nuclear explosion and meteorite impact.

This paper was published in *PNAS* and featured in *Nature Materials* and http://phys.org/.

1.7. Development and application of phase field approaches to study phase transformations, plastic flow, and their interaction at the nanoscale

1.7.1 Development of phase-field theory for martensitic phase transformations at large strains [4]

General phase-field theory for multivariant martensitic phase transformations and explicit models are formulated at large strains. Each order parameter is unambiguously related to the transformation strain of the corresponding variant. Thermodynamic potential includes energy related to the gradient of the order parameters that mimics the interface energy. Application of the global form of the second law of thermodynamics resulted in the determination of the driving force for change of the order parameters and the boundary conditions for the order parameters. Kinetic relationships between the rate of change of the order parameters and the conjugate driving force lead to the Ginzburg-Landau equations. For homogeneous fields, conditions for instabilities of the equilibrium states (which represent criteria for the phase transformation between austenite and martensitic variants and between martensitic variants) are found for the prescribed Piola-Kirchoff stress tensor. It was proved that these criteria are invariant with respect to change in the prescribed stresses. The expression for the rigid-body rotation tensor is derived for the prescribed Piola-Kirchoff stress. The explicit expressions for the Helmholtz free energy and for transformation strain in terms of order parameters are derived for the most general case of large elastic and transformational strains, rotations, as well as nonlinear, anisotropic, and different elastic properties of phases. For negligible elastic strains, explicit expression for the Gibbs potential is formulated. Results are obtained for fifth- and sixth-degree potentials in Cartesian order parameters and for similar potentials in hyperspherical order parameters. Geometric interpretation of transformation conditions in the stress space and similarity with plasticity theory are discussed. All material parameters are obtained for cubic to tetragonal transformation in NiAl. Phase transformations in NiAl, boron nitride, and graphite to diamond under uniaxial loading are described explicitly, and the importance of geometrically nonlinear terms is demonstrated.

A similar approach can be applied for twinning, dislocations, reconstructive transformations, and fracture.

1.7.2 Development of the numerical algorithms and phase-field simulation of stress-induced martensitic phase transformations at large strains [5]

A complete system of coupled phase-field and mechanical equations for the simulation of multivariant martensitic phase transformations at large strains is formulated. The finite-element approach and an algorithm for the solution of corresponding problems are developed and implemented in a code FIDESYS. Cubic to tetragonal phase transformation in NiAl is studied. Various problems on stress-induced nucleation and evolution of martensitic variants in nanosize samples are solved, including a rectangular sample with single and multiple circular or elliptical nanovoids (with and without surface tension), as well as nanotube and beam. Importance of finite

strain formulation is demonstrated. In particular, for the case when structural instability (buckling) of a beam is caused by phase transformation, for a geometrically linear formulation, phase transformation is suppressed. This is because finite rotation increases the energy of the system, while in a geometrically nonlinear theory energy is independent of rotation. Similar phase field and numerical approaches can be applied for twinning, dislocations, and reconstructive transformations.

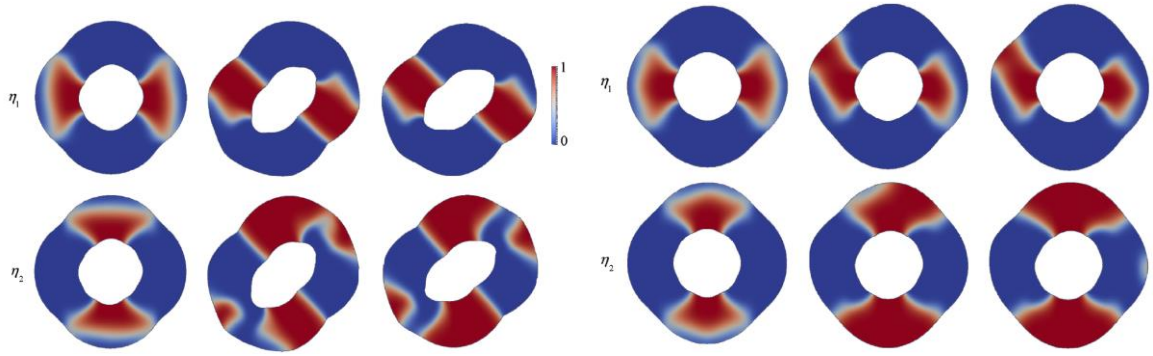

Fig. 7. Evolution of the first (upper row) and the second (lower row) martensitic variants (red color) in a nanotube in geometrically nonlinear (left) and linear (right) formulations.

1.7.3 Thermodynamically consistent phase field approach to phase transformations with interface stresses. Exact Analytical Results [3,6].

Thermodynamically consistent phase field theory for multivariant martensitic transformations is developed with the main focus on introducing correct *interface stresses (tension)*. The nontrivial point is that the interface tension (physical phenomenon) is introduced with the help of some geometric nonlinearities, even when strains are infinitesimal. Total stress at the diffuse interface consists of elastic and dissipative parts (that are determined by the solution of the coupled system of phase field and viscoelasticity equations) and the introduced interface stresses. An explicit expression for the free energy is derived that results in the desired expression for the interface stresses consistent with the sharp interface for the propagating nonequilibrium interface. Analytical expressions for nonequilibrium interface energy, width, entropy excess, as well as distribution of the interface tension are derived and parametrically studied. Interface stress tensor distribution is also obtained and analyzed for a critical martensitic nucleus. Possibility of extension of the developed approach to other phenomena and more general models is discussed.

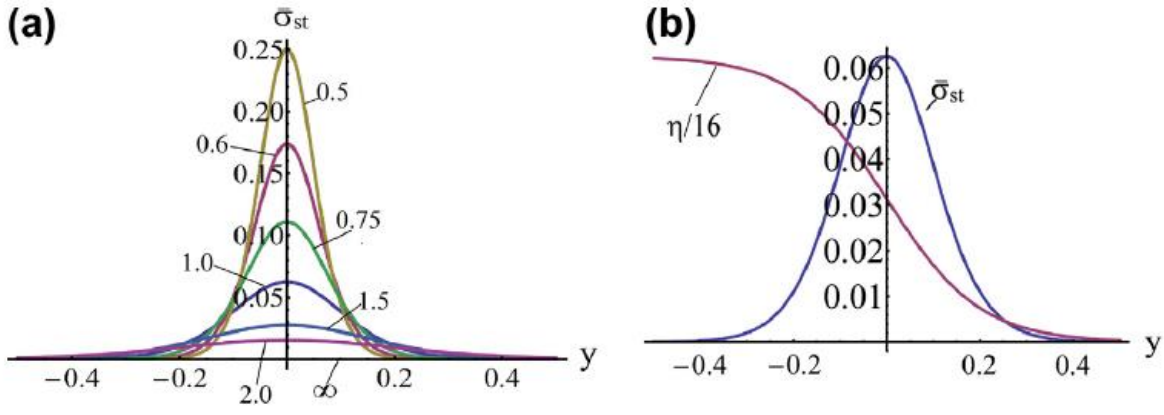

Fig. 8. (a) Distribution of the dimensionless biaxial surface tension for the nonequilibrium interface for several dimensionless interface widths shown near curves. (b) Superposed plots of the interface profile and dimensionless interface tension.

1.7.4 Multiple twinning and variant-variant transformations in martensite: Phase-field approach [12]

A phase field theory of transformations between martensitic variants and multiple twinning within martensitic variants is developed for large strains and lattice rotations. It resolves numerous existing problems. The model, which involves just one order parameter for the description of each variant-variant transformation and multiple twinnings within each martensitic variant, allows one to prescribe the twin interface energy and width, and to introduce interface stresses consistent with the sharp interface limit. A finite element approach is developed and applied to the solution of a number of examples of twinning and combined austenite-martensite and martensite-martensite phase transformations and nanostructure evolution in a nanosize sample. In particular, they include indentation and double indentation problems and reproduced three types of nontrivial experimentally observed microstructures involving finite rotations, including tip splitting and bending and twins crossing. A similar approach can be developed for electric and magnetic PTs.

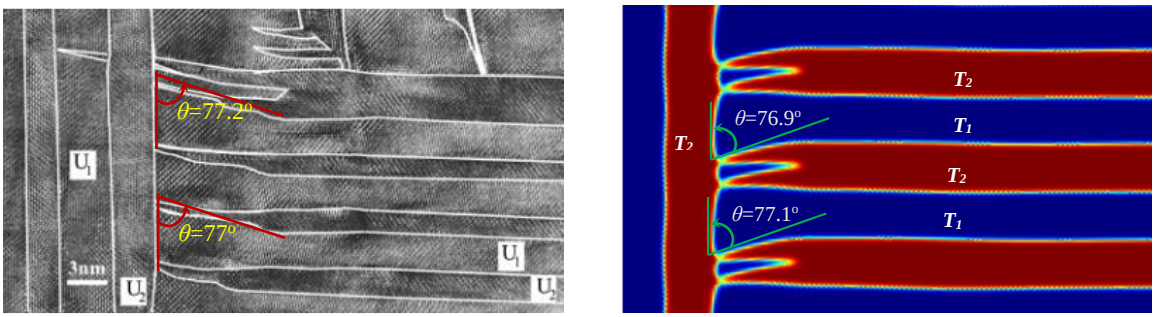

(a)

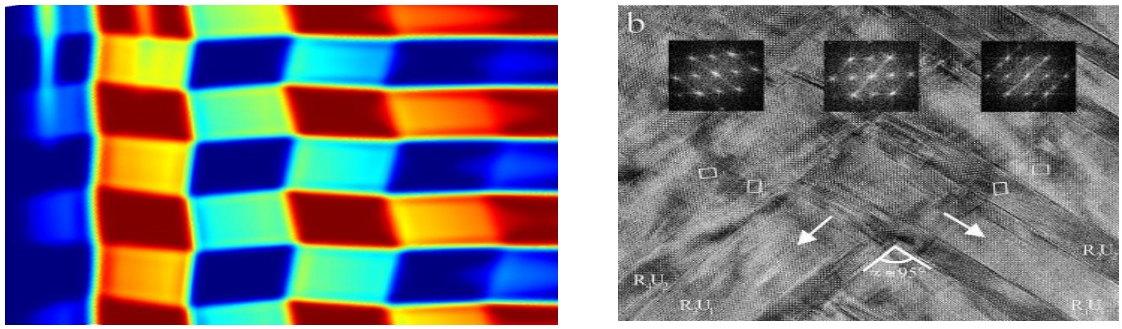

(b)

Fig. 9. Comparison of transmission electron microscopy images of a nanostructures in NiAl alloy (Boullay et al., Phys. Rev. B 64, 144105, 2001) and zoomed part of simulation results. (a) Splitting and bending of twin tips; (b) crossing twins.

1.7.5 Advanced Phase-Field Approach to Dislocation Evolution [9,20,35]

A qualitatively new phase field approach to dislocation evolution is developed. In contrast to known approaches, it includes:

a) Fully large strain formulation.
b) New local thermodynamic potential is suggested that eliminates stress-dependence of the Burgers vector and reproduces desired local stress-strain curve.
c) This potential also defines the desired, mesh-independent, dislocation height for any dislocation orientation.
d) A gradient energy includes an additional term, which excludes localization of dislocation within height smaller than the prescribed dislocation height but does not produce artificial interface energy and dislocation widening.

A comprehensive paper [20] is published in which phase field approach to dislocations is formulated within modern framework of nonlinear continuum mechanics. Drawbacks of previous approaches are demonstrated. Finite element algorithm is developed. Problems for nucleation and evolution of multiple dislocations along the single and multiple slip systems, interacting dislocation systems, and the interaction of dislocations with an martensitic phase transformations are solved numerically. In particular, nucleation and evolution of dislocations at the sharp austenite - martensite interface and near martensitic lath have been studied. Combining the phase field approach to dislocations with our recently developed phase field approach to phase transformations, we revealed an unexpected scale effect in the athermal resistance to the austenite - martensite interface motion due to nucleated incoherency dislocations. In particular, for very small and large ratio of the width of phase interface and dislocation height, an athermal threshold and hysteresis unexpectedly disappear.

A similar approach can be developed for partial dislocations and expended for dislocation reactions and detailed interaction between phase transformations and plasticity.

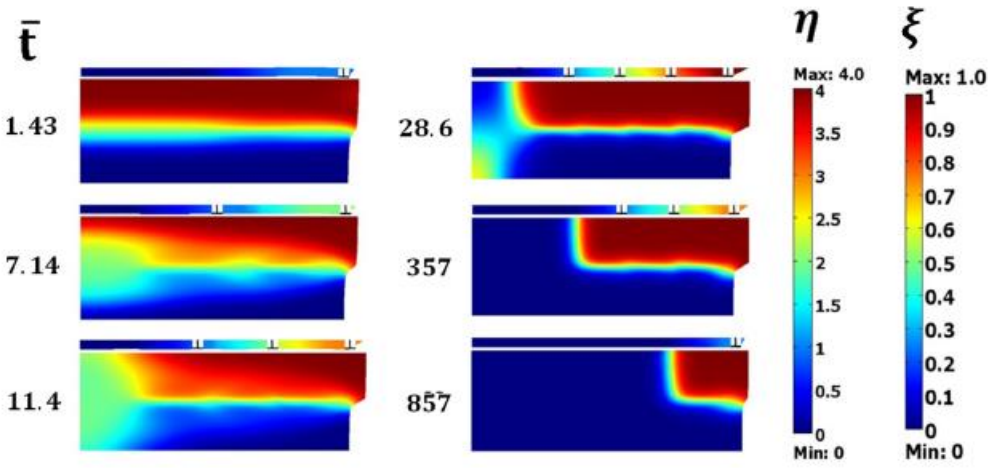

Fig. 10. Coupled evolution of the phase transformation order parameter η and corresponding dislocation order parameter ξ for initially coherent A-M interface in a half of a sample. Thin

band above the sample shows evolution of edge dislocations along the A-M interface. Finally, both martensite and misfit dislocations disappear.

In the final year, a comprehensive paper [35] on numerical approach and its mesh- and approximating FEM polynomial-independence, an analytical solution, and parameter identification using molecular dynamics results is published. Problems of nucleation and evolution of multiple dislocations along the single and multiple slip systems near martensitic lath, and along the sharp austenite-martensite interface, the activity of dislocations with two different orientations in a nanograined material under shear and pressure, and the interaction between two intersecting dislocation systems are studied. Surface-modified partial dislocation was revealed.

1.7.6 Phase field approach to interaction of phase transformation and dislocation evolution [2,22,23,26]

First phase field approach to coupled evolution of *martensitic phase transformations* and *dislocations* is developed as a synergistic combination of most advanced phase field approach for phase transformations and dislocations with additional coupling terms. Our theory is based on fully *geometrically nonlinear* formulation. Coupling between phase transformations and dislocations includes nonlinear kinematics and corresponding mechanical driving forces, *inheritance* of dislocations during phase transformations, and dependence of all material parameters for dislocations on the order parameter that describes phase transformations, which results also in the extra driving force for phase transformations due to change in dislocation energy during the phase transformations. Corresponding finite element method procedure is developed and applied to the following problems:

(a) Hysteretic behavior and propagation of an austenite - martensite interface with evolving incoherency dislocations for *temperature-induced* phase transformations. *Scale-dependent athermal hysteresis* is revealed and quantified and *mechanism* of interface motion through dislocation obstacles is revealed. These results can be utilized for controlling the region of metastability of phases.

(b) Evolution of phase and dislocation structures for *stress-induced* phase transformations. Dislocations are pushed by moving interface for small angle between slip direction and interface normal and penetrate through interface and are inherited by the product phase for large angles.

(c) Growth and arrest of martensitic plate for temperature-induced PT in a single and bicrystals. At higher temperature, dislocations arrest the plate, exhibiting athermal friction. When this friction can be overcome at lower temperature, width of the martensitic plate is larger than in the case without dislocations due to stress relaxation.

Results are presented as short letters [2,26] followed by two comprehensive papers with detailed theory [22] and finite element procedure and examples [23].

The interaction between phase transformations and dislocations drastically changes transformation thermodynamics, kinetics, and microstructure and is the most important basic and applied problem in the study of martensite nucleation and growth. Numerous applications include heat and thermomechanical treatment of materials to obtain desired structure and

properties; transformation-induced plasticity; synthesis of materials under high pressure and high pressure with large plastic deformations, e.g., during ball milling and in rotational diamond anvil cell; and phase transformations during friction, indentation, surface treatment, and projectile penetration.

Interaction between phase transformations and plasticity is also a key point in developing materials with high strength and ductility, in particular, utilizing transformation toughening.

A similar approach can be developed for the interaction of complete and partial dislocations with twins and diffusive phase transformations (described by Cahn-Hilliard theory), as well as electromagnetic and reconstructive phase transformations. Dislocation reactions, especially of inherited dislocations, can be included as well.

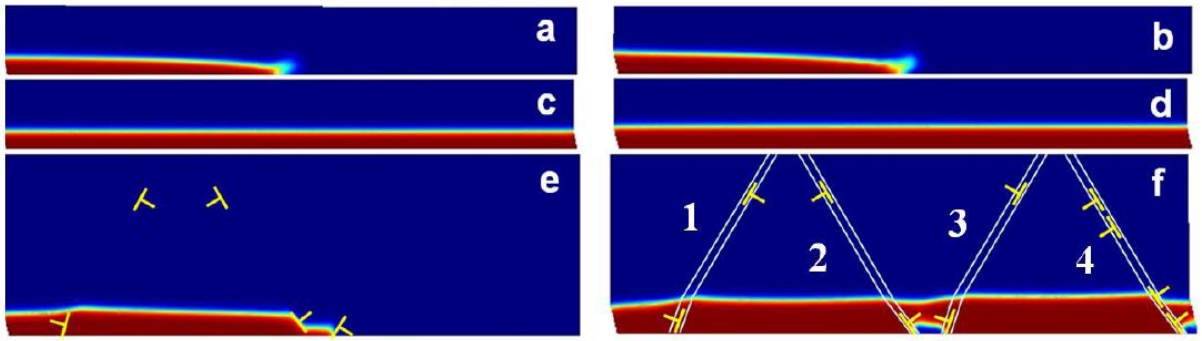

Fig. 11. Martensitic plate in the intermediate (a, b) and stationary (c, d) states for the thermal driving force X = 0.39 (left) and X= 0.49 (right) for the case without plasticity in a part of a rectangular sample. For the case with dislocations, the stationary solutions are shown in the entire sample with four slip planes, in the same scale as in (a)-(d), for X= 0.39 (e) and X= 0.49 (f).

1.7.7. Coupled phase transformation and dislocation evolution under pressure and shear in nanograin material: nanoscale mechanism of drastic reduction of transformation pressure [16,23]

Problem on coupled nucleation and evolution of dislocation and high pressure phase structures in the nanograin material under pressure and shear is solved utilizing the developed advanced PFA. Dislocations are generated at the grain boundaries and are densely piled up near them, creating a strong concentrator of the stress tensor. Averaged shear stress is essentially larger in the nanograin material due to grain boundary strengthening. This leads to the increase in the local thermodynamic driving force for PT, which allows one to significantly reduce the applied pressure. For all cases, the applied pressure is 3–20 times lower than the PT pressure and 2–12.5 times smaller than the phase equilibrium pressure. Plasticity plays a dual role: in addition to creating stress concentrators, it may relax stresses at same concentrators, thus competing with PT. Some ways to optimize the loading parameters have been found that lead to methods for controlling PT.

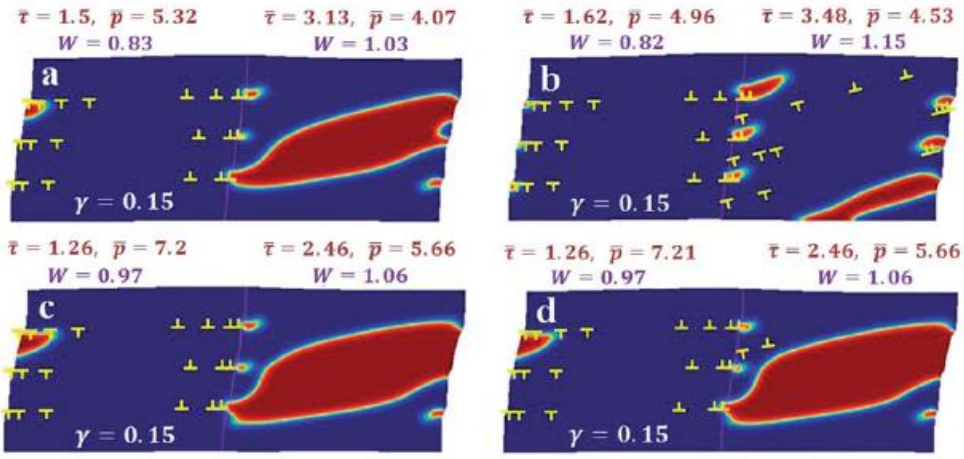

Fig. 12. Stationary distribution of high pressure phase (HPPs, red) and dislocations under compression and shear for gamma= 0.15. (a) Three dislocation systems are allowed in the left grain only and are pinned before PT starts. (b) In addition, in the right grain three dislocation systems inclined under 15^0 are included, which leads to the suppression of HPPs. (c and d) The same as in (a) and (b) but at higher pressure and lower shear stress. Even when plasticity in the right grain is allowed, just two dislocations appear, and PT to HPP is not suppressed.

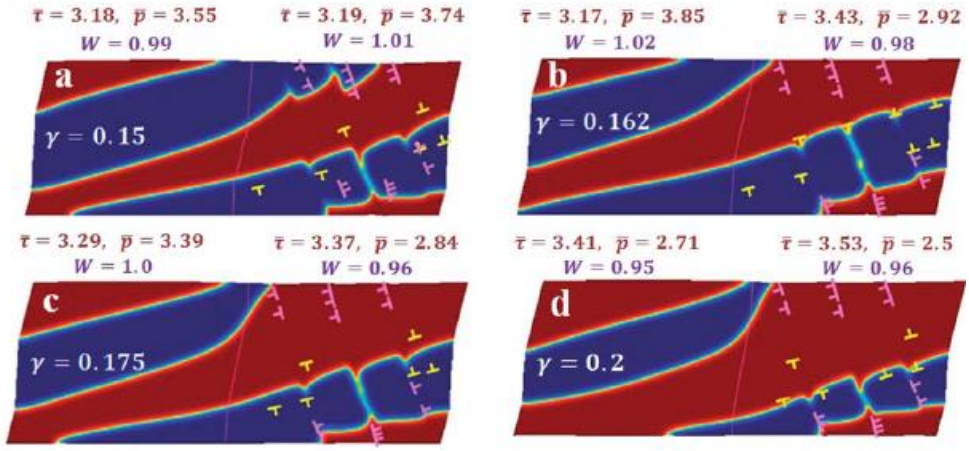

Fig. 13. Stationary distributions of HPPs and dislocations under growing shear, which approximately take into account grain rotation.

For better understanding of underlying physics, it is desirable to separate effects of pressure and plastic shear and to find both nanoscale detail and possibility of macroscale characterization of such PTs. Such a problem was solved in [23]. The final stationary morphology of HPP is governed by the local thermodynamic equilibrium (Fig. 14), either at the interfaces or in terms of stresses averaged over the HPP region or the entire grain. This is very surprising because of strong heterogeneity of stress fields and is in contrast to previous statements that phase equilibrium conditions do not enter the description of strain-induced PTs. These results give the

key idea on how to perform *scaling up* results of the nanoscale simulations to the microscale. It will be utilized in the future work.

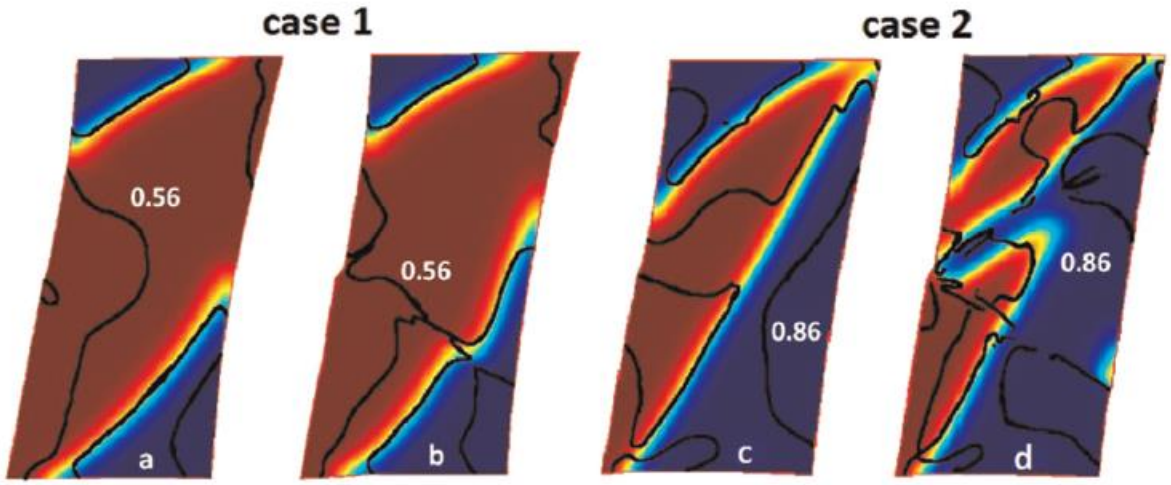

Fig. 14. Stationary phase state and contour line of the equilibrium transformation work for case 1 without (a) and with plasticity (b), and for case 2 without (c) and with plasticity (d). Interface positions coincide with the lines corresponding to the equilibrium PT work, both with and without plasticity.

1.8 Solid–solid transformations via nanoscale intermediate interfacial phase: Multiple structures, scale and mechanics effects [17,18]

Solid-solid (SS) phase transformations via nanometer size virtual or intermediate melt (IM) within the SS interface, hundreds of degrees below melting temperature, were predicted thermodynamically and are consistent with experiments for various materials. A necessary condition for the appearance of IM, using a sharp interface approach, was that the ratio of the energies of SS and solid-melt (SM) interfaces $k_E > 2$. Here, an advanced phase-field approach coupled with mechanics is developed that reveals various new scale and interaction effects and phenomena. Various types of IM are found: (a) continuous and reversible premelting and melting; (b) jump-like barrierless transformation to IM, which can be kept at much lower temperature even for $k_E < 2$; (c) unstable IM, i.e., a critical nucleus between SS interface and IM. A surprising scale effect related to the ratio of widths of SS and SM interfaces is found: it suppresses barrierless IM but allows keeping IM at much lower temperature and even for $k_E < 2$. Relaxation of elastic stresses strongly promotes IM, which can appear even at $k_E < 2$ and retained at $k_E = 1$. Developed theory can be adjusted for the diffusive phase transformations, formation of intergranular and interfacial phases, and surface-induced phase transformations.

Simulations are performed for $\beta \rightarrow \delta$ phase transformations (PTs) via IM in HMX energetic material. Obtained energy - IM width dependence is described by generalized force-balance models for short- and long-range interaction forces between interfaces but not far from the melting temperature. New force-balance model is developed, which describes phase field results even 100 K below the melting temperature. The effects of the ratios of width and energies of solid-solid and solid-melt interfaces, temperature, and the parameter characterizing

interaction of two solid-melt interfaces, on the structure, width, energy of the IM and interface velocity are determined by finite element method.

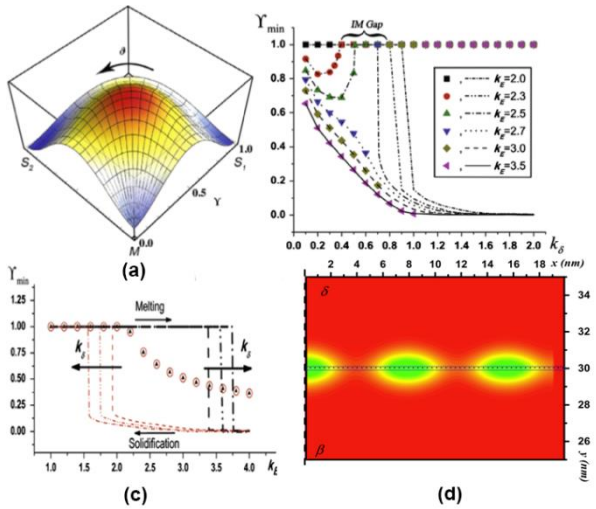

Fig. 15. (a) The 3D plot of the develop potential vs. profile of the radial order parameter $\Upsilon(z)$ and angular order parameter $\vartheta(z)$. Effect of interface width ratios k_δ (b), and interface energy ratio k_E (c) on the formation of IM are shown. Formation of multiple periodic critical nuclei is captured. (d).

1.9. Phase-Field Approach to Solid-Solid Phase Transformations via Intermediate Interfacial Phases under Stress Tensor [21,25,29]

The effect of elastic energy on nucleation and disappearance of a nanometer size intermediate melt (IM) region at a solid–solid (S_1S_2) phase interface at temperatures 120 K below the melting temperature is studied using a phase-field approach. A thermodynamically consistent phase-field (PF) potential for PTs between three different phases is developed with correct stresses and interface interactions, which satisfies all the thermodynamic instability and equilibrium conditions. An interaction between two SM interfaces via an IM, which plays a key role in defining a well-posed problem and mesh-independent solution, is captured using a special gradient energy term. Results are obtained for broad range of the ratios of S_1S_2 to solid–melt interface energies, k_E, and widths, k_δ. It is found that internal stresses only slightly promote barrierless IM nucleation but qualitatively alter the system behavior, allowing for the appearance of the IM when $k_E < 2$ (thermodynamically impossible without mechanics) and elimination of what we termed the IM-free gap.

It is shown that the elastic energy promotes the formation and retaining of IM and its structure, hundreds of degrees below the melting temperature, and also increases the interface velocity and width of IM. Remarkably, when mechanics is included within this framework, there is a drastic (16 times for HMX energetic crystals) reduction in the activation energy of IM critical nucleus. Two different critical nuclei are found: one is the IM nucleus in the SS interface, CN_1, and the other is SS nucleus in the S_1MS_2 interface, CN_2. A kinetic nucleation criterion is met and thermally activated melting occurs under conditions consistent with experiments for HMX when the elastic energy is included in the model, elucidating what had been to date mysterious

behavior. Similar effects are expected to occur for other material systems where S_1S_2 phase transformations via IM take place, including electronic, geological, pharmaceutical, ferroelectric, colloidal, and superhard materials.

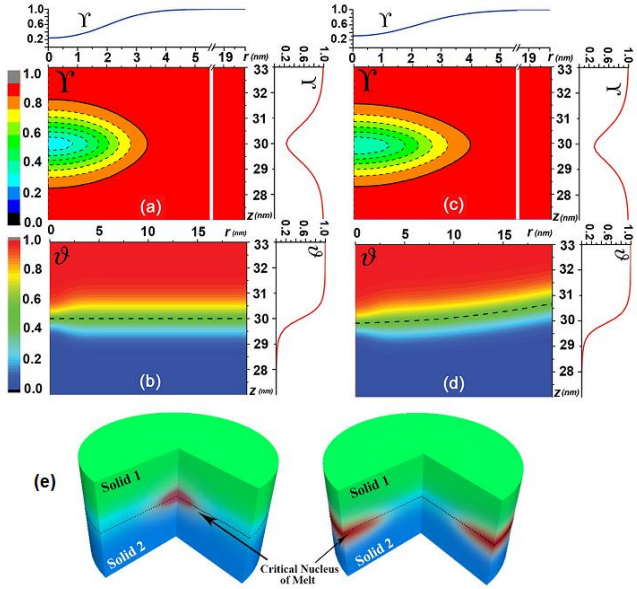

Fig. 16. Structure for the CN_1 with IM at the center of a sample. Simulations are performed at θ_e = 432 K, k_δ = 0.7, and k_E = 2.6 for the cases without (a,b) and with mechanics (c,d). Profile of the radial order parameter $\Upsilon(r)$ along the horizontal line z = 30 nm is plotted in the top insets. Vertical insets show the profile of the radial order parameter $\Upsilon(z)$ (top plots) and angular order parameter $\vartheta(z)$ (bottom plots) at r = 0. Solid line in the Υ lots corresponds to Υ = 0.9 and determines the boundary of disordered CN of IM within the S_1S_2 interface. (e) The 3D plot of the CN_1 and CN_2. Dotted line in the ϑ plots indicates the level line of ϑ = 0.5 and corresponds to the sharp S_1S_2 interface.

In the final year, results have been generalized for the case when interfacial stresses are taken into account, with solution of the similar problems [29].

1.10 Thermodynamically consistent phase field approach to phase transformations with interface stresses [3], [19]

A general continuum thermodynamic derivation of the main equations of the phase field approach to multivariant martensitic phase transformations is developed for both small strain [3] and large strain [19] problems. The main focus was on the consistent introduction of the interface stress tensor that transforms to biaxial tension with a magnitude equal to the interface energy for the non-equilibrium propagating interface. It was justified that the gradient of the order parameters in the gradient energy should be evaluated in the deformed state and the gradient energy and double-well part of the potential should be multiplied by ratio of mass densities in the undeformed and deformed states. For the case of a propagating plane interface, the expression for surface stresses reduces to biaxial tension with the force per unit area equal to the surface energy γ, providing the desired correspondence with a sharp-interface approach. This was achieved by utilizing an analytical solution for the nonequilibrium propagating austenite-

martensite interface and determining its energy γ. The nontrivial point in the derivation is that in order to introduce the interface stresses, one has to include some geometrically nonlinear terms even if deformations are infinitesimally small. Thus, a physical phenomenon such as interface tension is introduced with the help of geometrical nonlinearity. It was also found that the interface stresses do not contribute explicitly to the Ginzburg-Landau equations. However, they change elastic stresses, which significantly affect the Ginzburg-Landau solutions.

For the large strain formulation, the explicit expression for the Ginzburg-Landau equations have been found for fully geometrically nonlinear formulation, which was simplified for various geometrical approximations of smallness of some strain components and rotations. An important point in the current approach is that the elastic energy is defined per unit volume of unloaded (intermediate) configuration, in which elastic properties are usually determined in experiment and atomistic simulations. Such a choice leads to the correct expression for the elasticity rule and additional contributions to the Ginzburg-Landau equations and expression for the entropy.

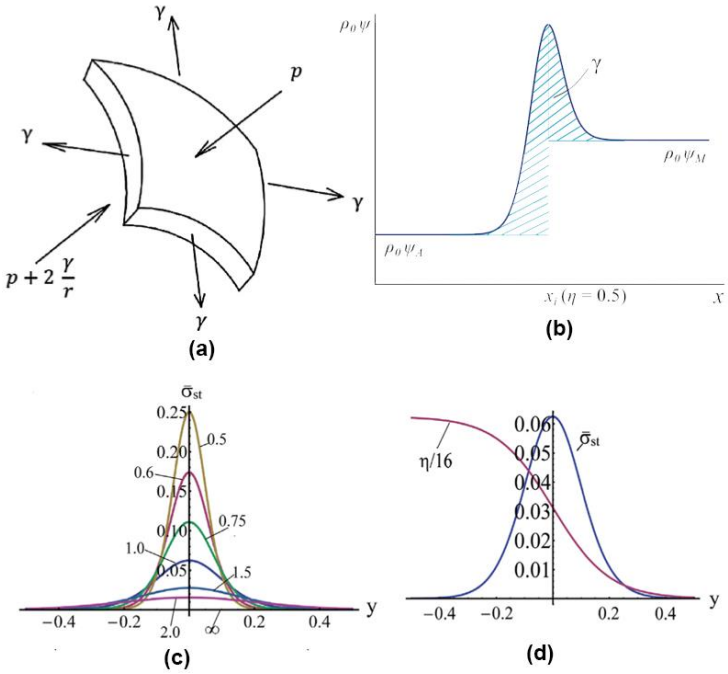

Fig. 17. (a) A material surface is subjected to a biaxial tension with a magnitude equal to the surface energy γ. (b) Schematic for definition of the energy γ for nonequilibrium interface. (c) Distribution of the dimensionless biaxial surface tension $\bar{\sigma}_{st}$ for the nonequilibrium interface for several dimensionless interface widths $\tilde{\delta}$. (d) Superposed plots of the interface profile $\eta(y)/16$ and dimensionless interface tension $\bar{\sigma}_{st}$ for the dimensionless interface $\tilde{\delta}$=1.

In the final year, interfacial stresses have been introduced for anisotropic interface energy [28,32] and multiphase interfaces [29].

1.11 Unambiguous Gibbs dividing surface for nonequilibrium finite-width interface: Static equivalence approach [15]

A strict solution to the longstanding problem in the interface and surface science, formulated by Gibbs, is found: how to define the position of the sharp interface equivalent to the finite-width interface. We utilized the principle of static equivalence and even obtained two solutions, which fortunately coincide at least for the phase field model considered here. It is also consistent with the expression for the velocity of the curved sharp interface. The next question is whether this is the case for other phase field polynomials and theories and whether there is a way to prove the equivalence of both conditions for an arbitrary thermodynamic potential. Note that the principle of static equivalence is the fundamental principle of mechanics (and, consequently, physics) and it must not be violated. It is surprising that it was neglected in the interface and surface science.

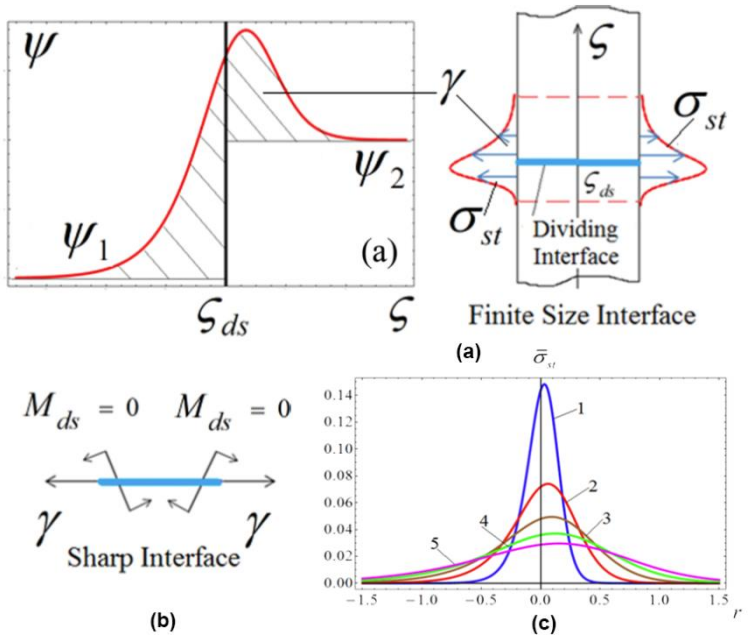

Fig. 18. (a) Distribution of the free energy across a nonequilibrium interface and definition of an interface excess energy as an area of dashed regions. (b) Principle of static equivalence of distributed interface stresses for a finite-width interface and the resultant force placed at the dividing surface. (c) Distribution of the dimensionless biaxial interface stress $\bar{\sigma}_{st}$ for the nonequilibrium interface for different interface widths δ.

1.12 Multiple phase field theory for temperature- and stress-induced phase transformations [24,36]

A critical outstanding problem on developing of phase field approach for temperature- and stress-induced phase transformations between arbitrary *n* phases is solved. PFA for multiphase materials, which with high and controllable accuracy satisfy all the desired conditions for arbitrary *n* phases, is developed. Instead of explicit constraints on the order parameters, we included in the simplest potential the terms that penalize the deviation of the trajectory in the order parameter space from the straight lines connecting each of the two phases. It describes each of the PTs with the single order parameter, which allows us to use an analytical solution for the

propagating interface to calibrate each interface energy, width, and mobility. It reproduces the desired PT criteria via instability conditions; introduces interface stresses, and allows us to control the presence of the third phase at the interface between the two other phases. Finite-element simulations exhibit very good correspondence with results based on the exact three-phase model [12] (which, however, cannot be generalized for $n>3$) and with nontrivial experimental nanostructure, both shown in Fig. 9. The developed approach unifies and integrates approaches developed in different communities (in particular, solidification and martensitic PTs) and is applicable to various PTs between multiple solid and liquid phases and grain evolution, and can be extended for diffusive, electric, and magnetic PTs.

In the final year, much more detailed analysis has been performed [36] for multiphase temperature-induced PTs with application to solid-solid PTs via nanometer size virtual or intermediate melt within the SS interface, hundreds of degrees below melting temperature. Simulations were performed for $\beta \rightarrow \delta$ PTs via intermediate melt in HMX energetic material.

In the final year (1.13-1.15):

1.13. Thermodynamically consistent phase field theory of phase transformations with anisotropic interface energies and stresses [28,32].
The main focus here is to introduce, in a thermodynamically consistent manner, an anisotropic interface energy into a phase field theory for PTs. Previous theories have assumed the free energy density (i.e., gradient energy) is an anisotropic function of the gradient of the order parameters in the current (deformed) state, which yields a nonsymmetric Cauchy stress tensor. This violates two fundamental principles: the angular momentum equation and the principle of material objectivity. Here, it is justified that for a noncontradictory theory the gradient energy must be an isotropic function of the gradient of the order parameters in the current state, which also depends anisotropically on the direction of the gradient of the order parameters in the reference state. A complete system of thermodynamically consistent equations is presented. We find that the main contribution to the Ginzburg-Landau equation resulting from small strains arises from the anisotropy of the interface energy, which was neglected before. The explicit expression for the free energy is justified. An analytical solution for the nonequilibrium interface and critical nucleus has been found and a parametric study is performed for orientation dependence of the interface energy and width as well as the distribution of interface stresses.

1.14. Modeling and simulations in samples with large elastoplasticity under extreme pressures in a diamond anvil cells [30].
In high pressure research, static megabar pressures are typically produced by compression of a thin sample by two diamonds in various types of diamond anvil cells. This process is accompanied by large plastic deformation (sample thickness is reduced by a factor of 30 in Fig. 20a), and finite elastic deformation of a sample and even the diamond. A thermodynamically consistent system of equations for large elastic and plastic deformation of an isotropic material obeying nonlinear elasticity and pressure dependent yield condition is formulated. The Murnaghan elasticity law and pressure-dependent J_2 plasticity are utilized. The finite-strain third-order elasticity law for cubic crystals is utilized for diamond. A computational algorithm is presented with emphasis on the stress update procedure and derivation of the consistent tangent moduli. It is implemented as a user material subroutine in the finite element code ABAQUS.

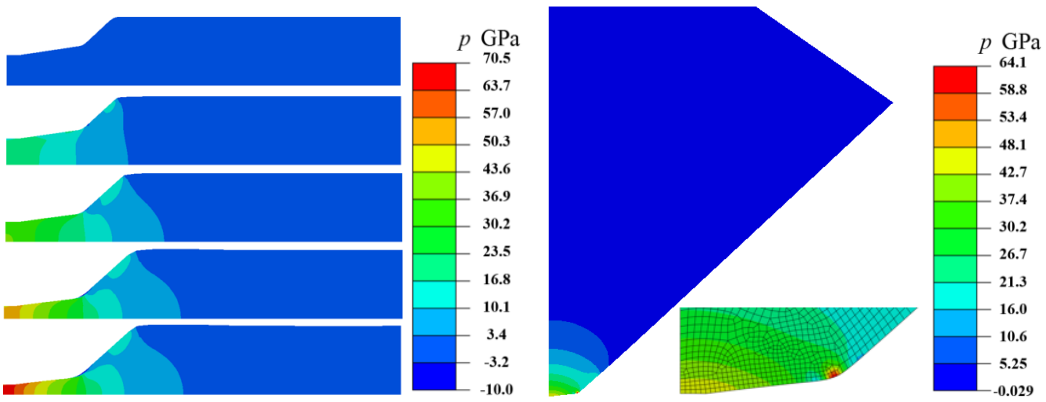

(a) (b)

Fig. 19. Distribution of the pressure in the sample (a) and diamond (b). In (a), the applied force grows from the top to bottom, and in Fig (b) diamond pressure filed corresponds to the case when the maximum pressure in sample reaches 70.5 GPa.

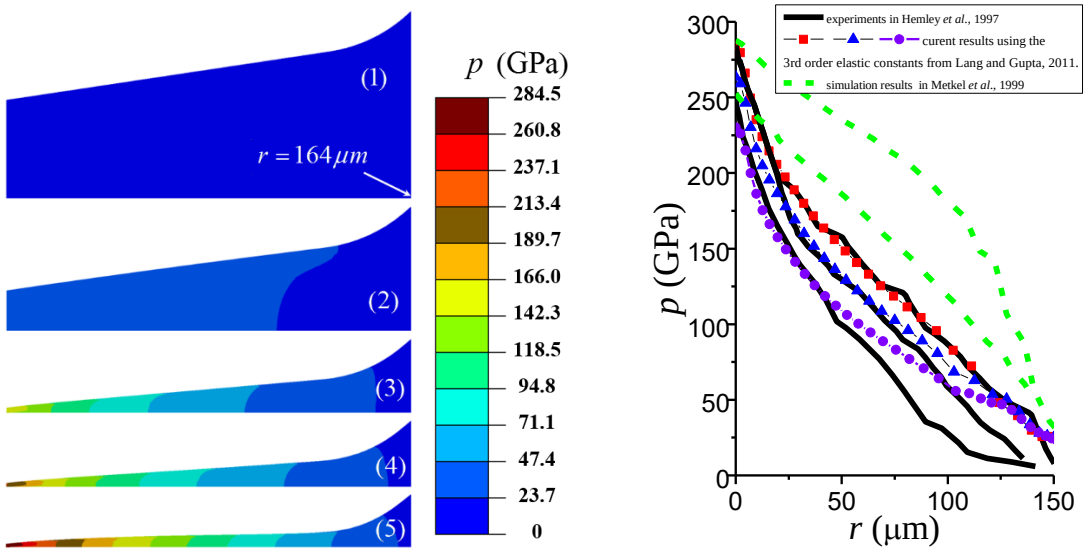

(a) (b)

Fig. 20 Pressure distribution in the sample $(0 \le r \le 164\mu m)$ and contact surface of sample with an increasing applied normal stress σ_n. In (a), the normal stress σ_n is 0 (1), 1.022 GPa (2), 1.652 GPa (3), 1.903 GPa (4), and 2.546 GPa (5).

Material parameters for a rhenium sample, as an example, and a diamond are calibrated based on the experimental and atomistic simulation results in the literature. The evolution of the stress and strain tensor fields in the sample and diamond is studied up to a pressure of 300 GPa (Fig. 19 and 20). Good correspondence between numerical and experimental pressure distributions at the diamond-sample contact surface is obtained (in Fig. 20b). Because there is a significant scatter of the magnitude of reported third-order single-crystal elastic moduli for diamond, their effect on

strains and stresses is studied in detail. With the smaller third-order elastic moduli, the phenomenon of cupping of the diamond-sample contact surface is reproduced, which plays an important role in increasing maximum pressures for a given anvil geometry. The results provide important insight into the mechanical response in diamond anvil cells, interpretation of materials properties under extreme conditions from heterogeneous fields, and optimum design of cells for reaching the maximum static pressure in a volume sufficient for the desired measurements.

1.15. Effects of gasket on coupled plastic flow and strain-induced phase transformations under high pressure and large torsion in a rotational diamond anvil cell [31]

Combined plastic flow and strain-induced PTs under high pressure in a sample within a gasket subjected to three dimensional compression and torsion in a RDAC are studied using a finite element approach. The results are obtained for the weaker, equal-strength, and stronger high-pressure phases in comparison with low-pressure phases. It is found that, due to the strong gasket, the pressure in the sample is relatively homogenous and the geometry of the transformed zones is mostly determined by heterogeneity in plastic flow in Fig. 21. For the equal-strength phases, the PT rate is higher than for the weaker and stronger high-pressure phases. For the weaker high-pressure phase, transformation softening induces material instability and leads to strain and PT localization. For the stronger high–pressure phase, the PT is suppressed by strain hardening during PT. The effect of the kinetic parameter *k* that scales the PT rate in the strain-controlled kinetic equation is also examined. In comparison with a traditional DAC without torsion, the PT progress is much faster in RDAC under the same maximum pressure in the

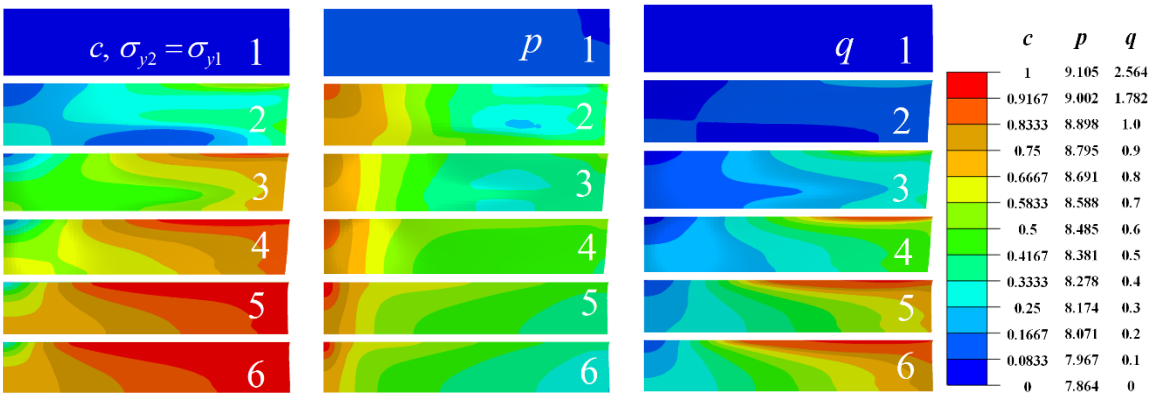

(a) (b) (c)

Fig. 21. Evolution of distributions of (a) concentration of the high-pressure phase *c*, (b) pressure *p*, and (c) accumulated plastic strain *q* fields in the sample, with increasing rotation angle φ under a constant compressive axial force *F*=6.19, for equal-strength phases $\left(\sigma_{y2}=\sigma_{y1}\right)$. Rotation angle φ is (1) 0, (2) 0.1, (3) 0.3, (4) 0.5, (5) 0.8, and (6) 1.0 radians.

sample. Finally, the gasket size and strength effects are discussed. For a shorter and weaker gasket, faster plastic flow in radial and thickness directions leads to faster PT kinetics in comparison with a longer and stronger gasket. The rates of PT and plastic flows are not very sensitive to the modest change in a gasket thickness. Multiple experimental results are reproduced and interpreted. Obtained results allow one to design the desired pressure-plastic

strain loading program in the experiments for searching new phases, reducing PT pressure by plastic shear, extracting kinetic properties from experiments with heterogeneous fields, and controlling homogeneity of all fields and kinetics of PTs.

2. Experimental Study

2.1 Compression and shear of nanostructured hBN and the lowest ever transformation pressure to wBN [8]

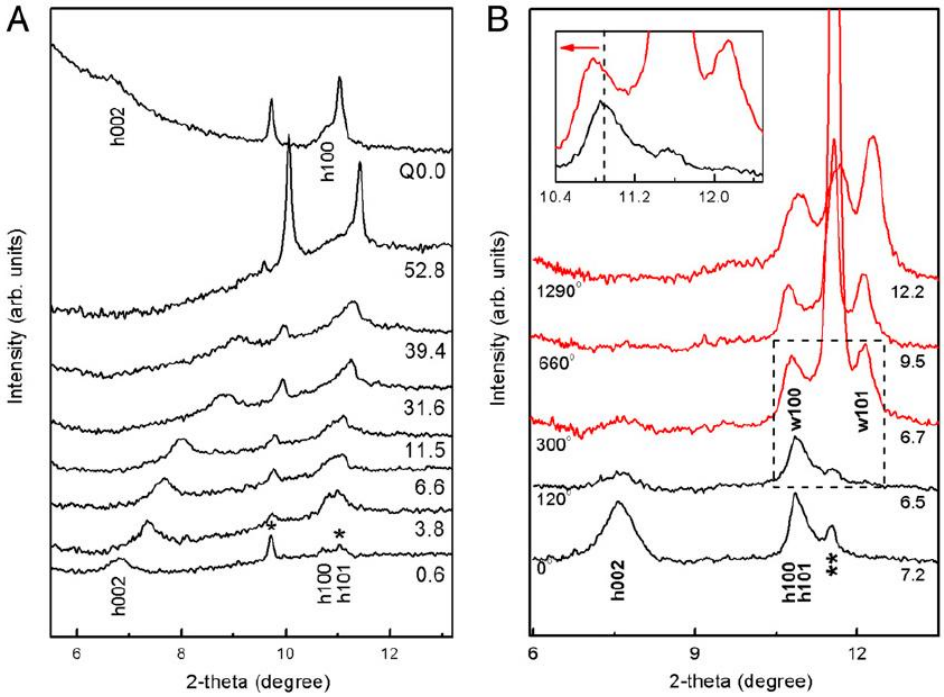

Fig. 20. (A) Selected high-pressure XRD patterns from run I for hydrostatic and quasi-hydrostatic cold compression of hBN in DAC. Numbers under the patterns are pressures in gigapascals, and Q represents quenched. The asterisk marks the diffraction peaks from the rhenium gasket. (B) Selected high-pressure XRD patterns from run II for compression and shear of hBN in RDAC. The lowest pattern was obtained at the center of the sample chamber, and other patterns were obtained 75 μm away from the center of the sample chamber. Angles of anvil rotation (in degrees) and pressures (in gigapascals) are noted below the patterns. The double asterisk marks the diffraction peak from the gasket [α-Fe (110) peak]. (Inset) Magnified view of the pattern enclosed in the dashed frame. The dashed line and arrow are visual guides.

Disordered structures of boron nitride (BN), graphite, boron carbide (BC), and boron carbon nitride (BCN) systems are considered important precursor materials for synthesis of superhard phases in these systems. However, phase transformation of such materials can be achieved only at extreme pressure–temperature conditions, which is irrelevant to industrial applications. Here, the phase transition from disordered nanocrystalline hexagonal (h)BN to superhard wurtzitic

(w)BN was found at room temperature under a pressure of 6.7 GPa after applying large plastic shear in a rotational diamond anvil cell(RDAC) monitored by in situ synchrotron X-ray diffraction (XRD) measurements. However, under hydrostatic compression to 52.8GPa, the same hBN sample did not transform to wBN but probably underwent a reversible transformation to a high-pressure disordered phase with closed-packed buckled layers. The current phase-transition pressure is the lowest among all reported direct-phase transitions from hBN to wBN at room temperature. Usually, large plastic straining leads to disordering and amorphization; here, in contrast, highly disordered hBN transformed to crystalline wBN. The mechanisms of strain-induced phase transformation and the reasons for such a low transformation pressure are discussed. Our results demonstrate a potential of low pressure–room temperature synthesis of superhard materials under plastic shear from disordered or amorphous precursors. They also open a pathway of phase transformation of nanocrystalline materials and materials with disordered and amorphous structures under extensive shear.

This paper is published in PNAS [8].

2.2 Compression and shear of B_4C: low pressure amorphization

Boron-rich materials are promising for their superhard and high-temperature properties and corresponding applications. Among these boron-rich complexes, boron carbide has recently attracted the interest of researchers and has been extensively studied [101-103]. It is one of the hardest materials; however, the shear strength drops significantly above 20GPa, which limited its applications in protection against external impact [104]. Shockwave experiments indicate that the shear softening is due to pressure-induced amorphization [103]. A number of reports of in-situ high pressure DAC experiments indicates that amorphous B_4C cannot be obtained under hydrostatic compression up to 50 GPa[105,106]. Recent results suggest that nonhydrostatic stress is a critical factor in pressure-induced amorphization. Also, amorphization of B_4C took place during decompression from a loading pressure above 26 GPa [104].

We performed the first exploratory experiments on behavior of B_4C under high pressure and severe plastic shear in RDAC, and characterized material using both by in situ X-ray diffraction and Raman scattering technique. We **discovered amorphization of B_4C under relatively low external stress**.

2.2.1 First run of experiment

We have begun to work on compression and shear of B_4C. At very low load (pressure lower than 1 GPa), we applied large shear on the sample. From the in situ synchrotron X-ray diffraction measurements, we found the gradual disappearance of diffraction peaks with application of shear. Yet we still can detect the diffraction peaks from B_4C after 1700 degrees of anvil rotation, even though they are very weak. This may be due to strong heterogeneity of plastic shear and pressure fields, which causes incomplete amorphization. Also SEM measurement indicated that the sheared sample after unloading contains the crystallized phase of B_4C, may be because amorphization is reversible (like we found for SiC). Thus, we believe that we revealed *strain-induced amorphization in B_4C under low pressure, probably reversible*.

2.2.2 Raman scattering measurements of sheared B_4C at high pressure

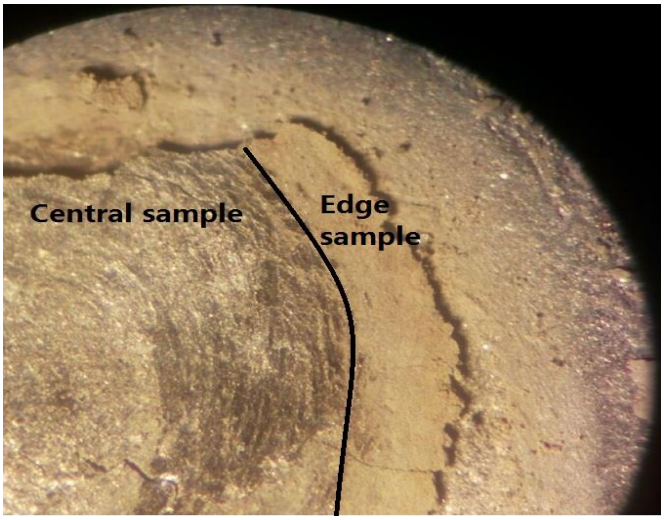

Fig. 21. Microscopic view of quenched B_4C

Fig. 21 A typical photo of sheared sample of B_4C in an RDAC. Sample can be divided into two regions, the relative dark one (the central region of the anvil, which is on the left side to the drawn curve in the figure), and the light color one (the edge region of the anvil, which is on the right of the drawn line).

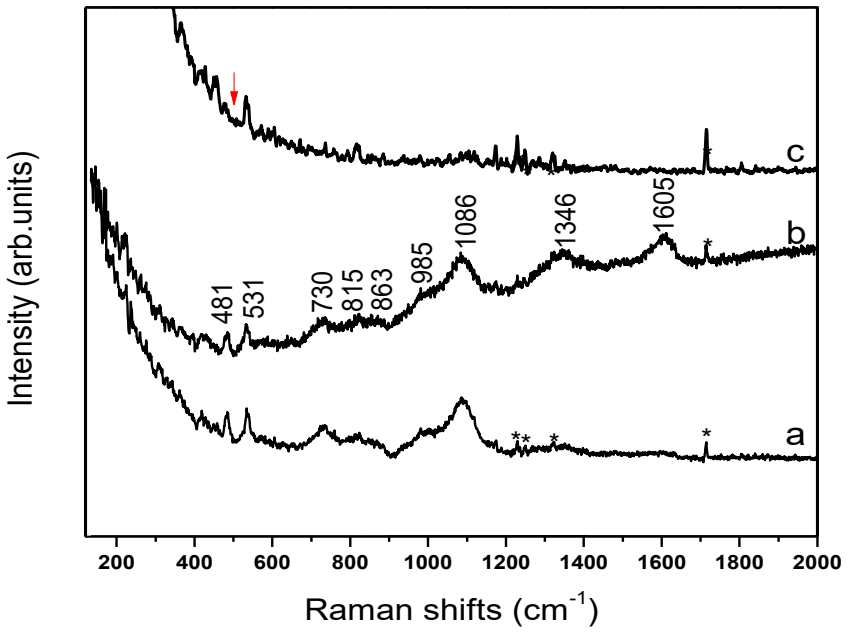

Fig. 22. Raman spectra of crystalline B_4C after compression and shear (quenched): (a) starting material; (b) quenched sample at the edge; and (c), quenched sample at the center.

The corresponding Raman spectra are shown in Fig. 22. The Raman spectrum of the sample at the edge (Fig. 22 (b)) has the fingerprint of the Raman D and G bands, which are located at 1346 and 1605 cm^{-1}. These are the characteristic Raman bands of an*amorphous* B_4C. The band at ~1810 cm^{-1}, which usually appears in an amorphous phase, is not observable. It may be too weak to be detectable.

The Raman spectrum from the central part of the sample has less Raman peaks than that of either a crystalline or the amorphous form at the edge of the sample. Moreover, the observation of the sharp peak at 531 cm^{-1} evidences the boron icosahedra molecular structure being still intact; while the disappearance of the peak at 481 cm^{-1}, which reflects the C-B-C stretching vibration, indicates that the breakdown of the C-B-C atomic chain resides in a crystalline B_4C.

Thus, we believe that the central part and the edge part of the sample both have phase transformation. But the phases are different, the phase at the edge is an amorphous phase; and the phase of the sample at the center part needs to be determined, most likely is another amorphous phase with different structure.

The phase uniformity of quenched sample at different positions was also studied by measuring the Raman scattering at the top surface and side of B_4C sample quenched from the RDAC. The top surface was the part that contacted the anvil surface and the side did not contact any material during the shear application, see Fig. 23.

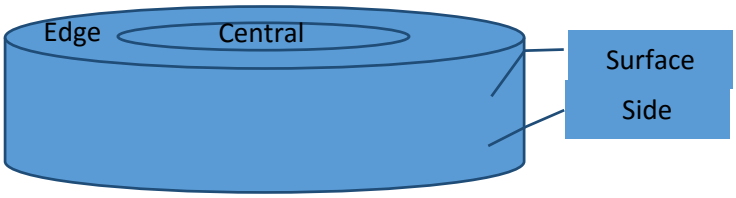

Fig. 23. The scheme of the sample

The Raman spectra of both surface and side quenched edge B_4C are shown in Fig. 24. The Raman signal of side edge sample is identical with that on top surface at the edge, indicating the transition completion along the thickness direction of the sample.

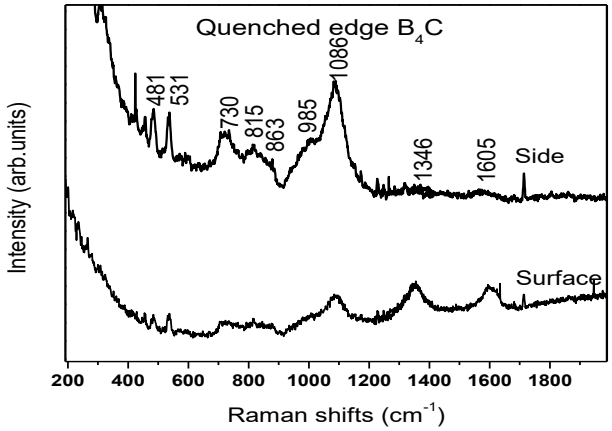

Fig. 24. The Raman spectra of side and surface region in quenched edge B_4C sample

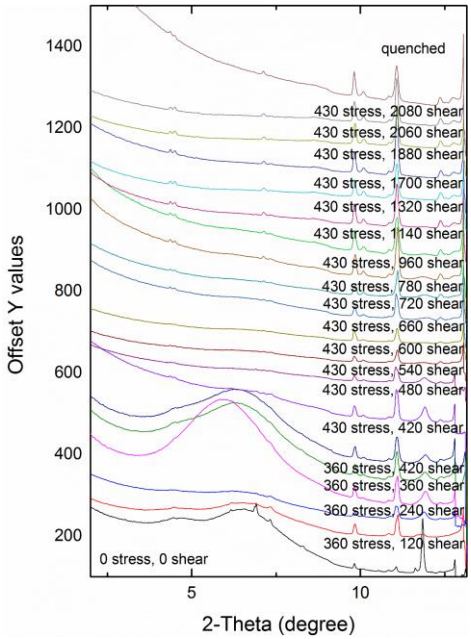

Fig. 25. Integrated X-Ray diffraction patterns for B_4C.

2.2.3 High pressure X-Ray diffraction of B_4C

In situ X-ray diffraction measurements of B_4C were also carried out in situ at high pressure and shear. Figs. 25 and 26 are the X-ray diffraction image after integration and the initial diffraction image of diffraction on the sample during processing of pressure and shear. The data are still under analysis and the analytical results will be reported later on. But one result can be ascertained that from the quenched pattern, we also observed the disappearance of the diffraction lines from crystalline B_4C.

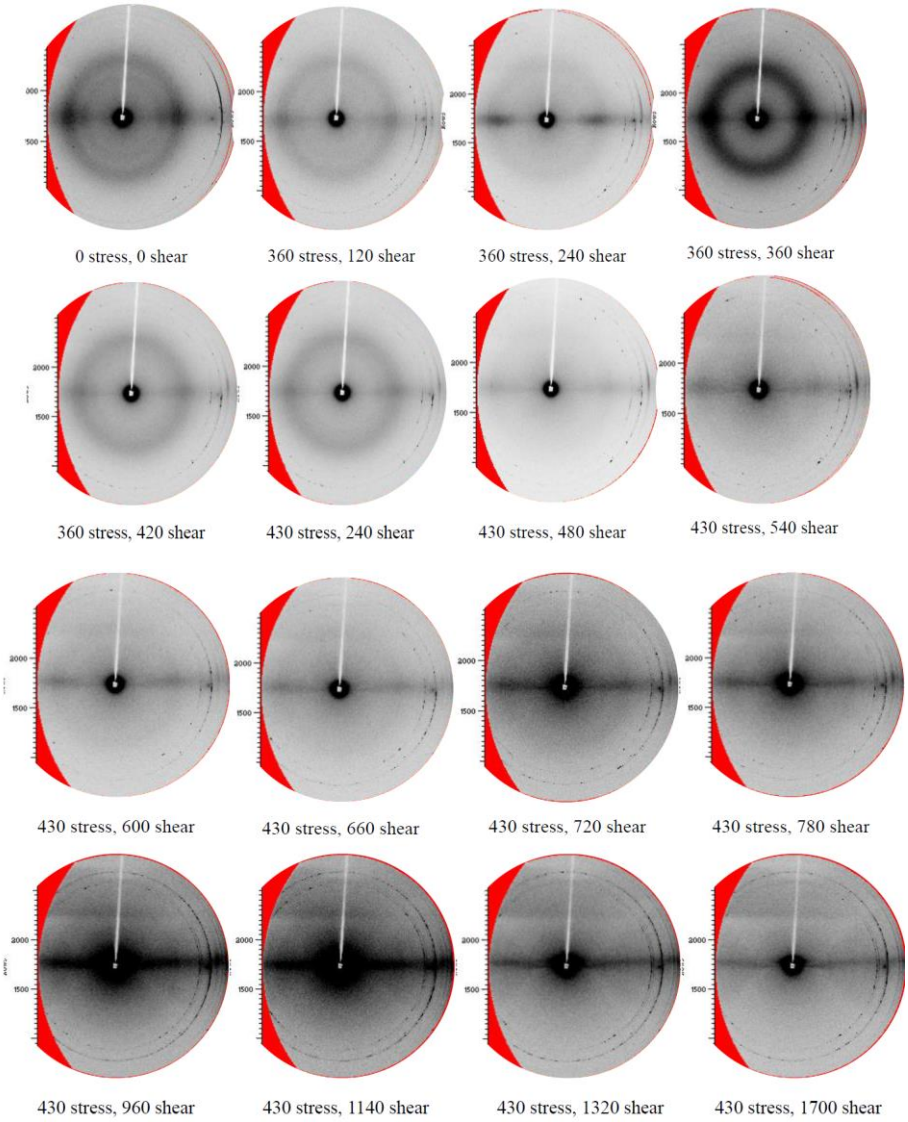

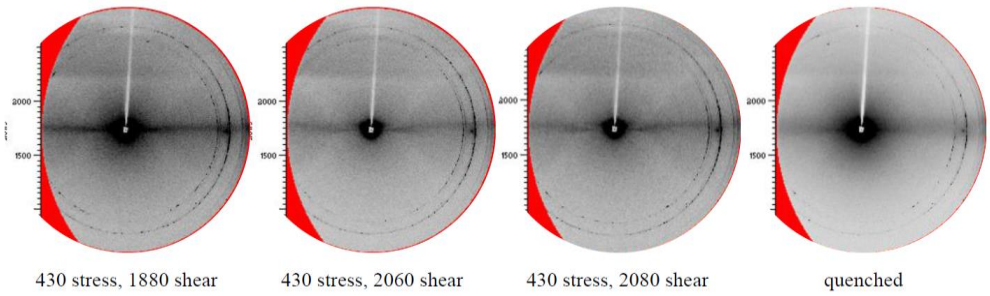

Fig. 26 X-ray diffraction image of B_4C at high pressures and shear. The number in stress is the rotation angle of screw for axial load application and the number of shear is the degree of angle rotation of a diamond.

2.2.4 Concluding remarks

From the present results, we conclude

1. Shear induces amorphization of B_4C.
2. There are at least two different amorphous phases (poly-amorphism).
3. In one of amorphous phases, the B_4C molecules are intact and the amorphization is initiated within the molecular B_4C.
4. In the other of amorphous phases, the C-B-C chain in crystalline B_4C is breakdown. It may lead to the breakdown of the B_4C molecule forming another type of material. It would be very interesting to further investigate this new type of B_4C.

2.2.5 References cited

101.Chen, M. W., McCauley, J.W. and Hemker, K. J. Shock-induced localized amorphization in boron carbide. Science 299, 1563-1566 (2003).

102.Domnich, V., Reynaud, S., Haber, R. A. and Chhowalla, M. Boron carbide: structure, properties, and stability under stress. J. Am. Ceram. Soc. 94, 3605–3628 (2011).

103. Reddy, K. M., Guo, J. J., Shinoda, Y., Fujita, T., Hirata, A., Singh ,J .P. McCauley, J. W. and Chen, M. W. Enhanced mechanical properties of nanocrystalline boron carbide by nanoporosity and interface phases. Nature Communications. 3, 1052, (2012)

104. Yan, X. Q., Tang, Z., Guo, J.J., Jin, C. Q., Zhang, Y., Goto, T., McCauley, J. W. and Chen, M. W.. Depressurization amorphization of single crystal boron carbide. Phys. Rev. Lett. 102, 075505 (2009).

105. Nelmes, R. J., Loveday, J. S., Wilson, R. M., Marshall, W. G.,Besson, J. M., Klotz, S., Hamel, G., Aselage, T. L. and Hull S. Observation of Inverted-Molecular Compression in Boron Carbide. Phys. Rev. Lett. 74, 2268 (1995)

106. Holmquist, T. J., Johnson, G. R. Characterization and evaluation of boron carbide for plate-impact conditions. Journal of Applied Physics, 100, 093525-093525-13 (2006).

2.3 Compression and shear of SiC

Using an anvil with diameter of 1mm and a sample chamber of 0.5-0.7mm, we compressed and sheared SiC. The pressure was very low, on the level of 0.1 GPa. We performed a 540° anvil rotation. Then we used a motor to applied shear for 28 min at a speed of 4.0 rotation/min. The grain size of SiC is 1μm in diameter. After the process, we could not observe the diffraction peaks from SiC. Then we took the sample for high resolution SEM study, and found that the SiC grain becomes much finer, yet it is still in the shape of a grain, i.e., in the crystalline form. Figs. 27 and beyond are the SEM analyses of the processed SiC (Zr found in the analysis served as the gasket in the process). Even though we did not identify a phase transition, we did observe significant microstructural changes in the sample. We thus need to further process and analyze the sample.

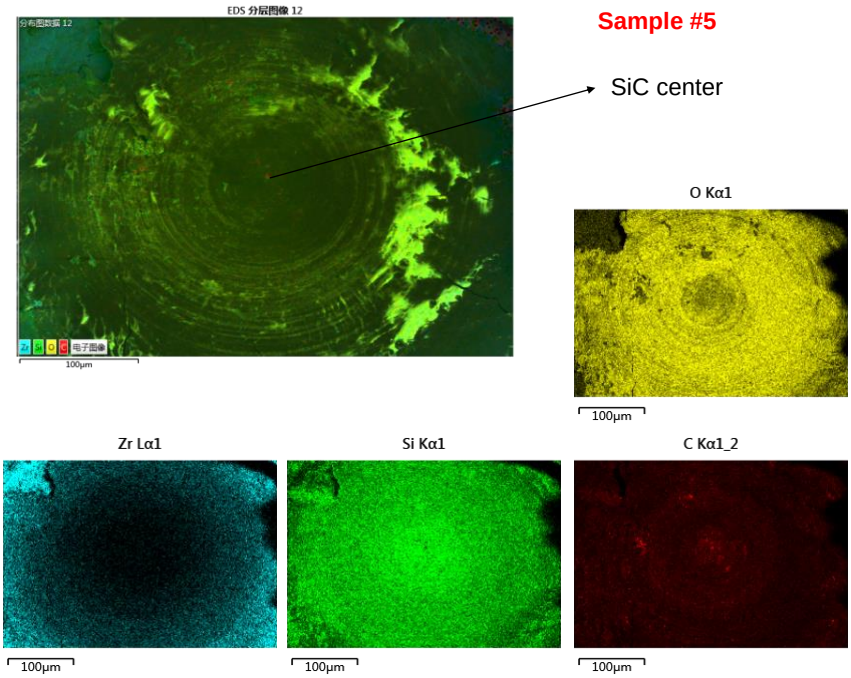

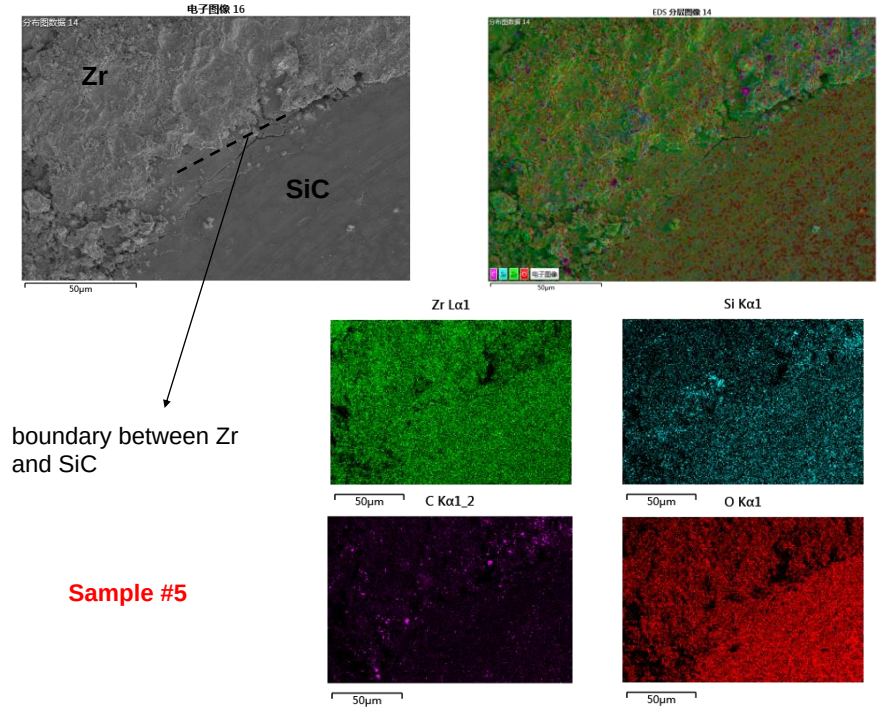

Fig. 27. SEM image of the processed SiC.

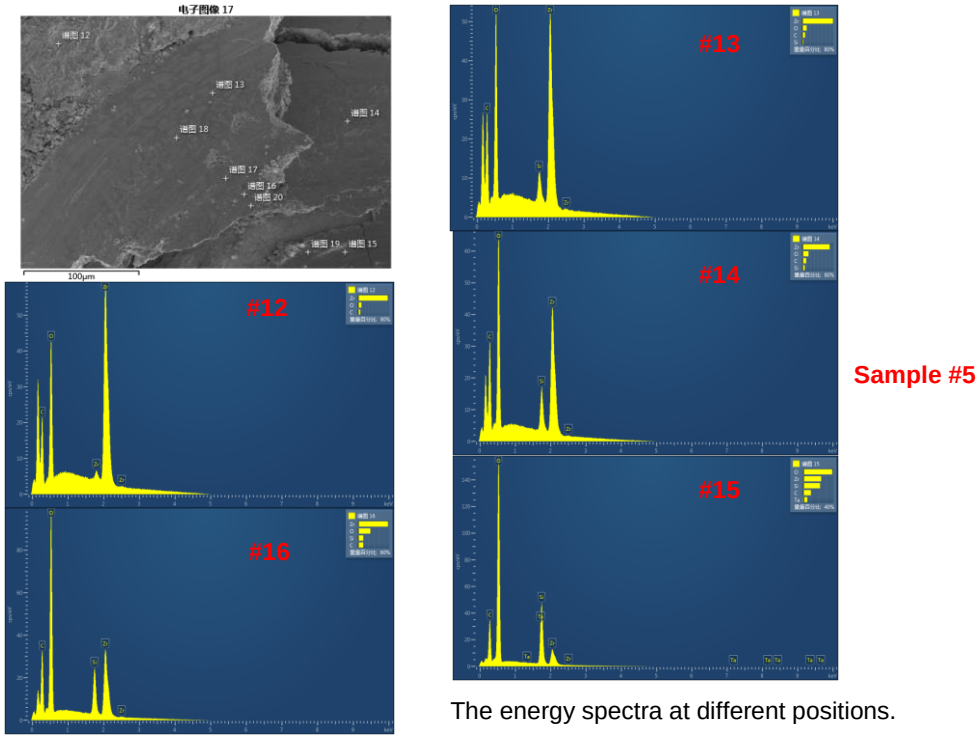

Fig. 28. Energy analysis to determine the distribution of each element (molecule).

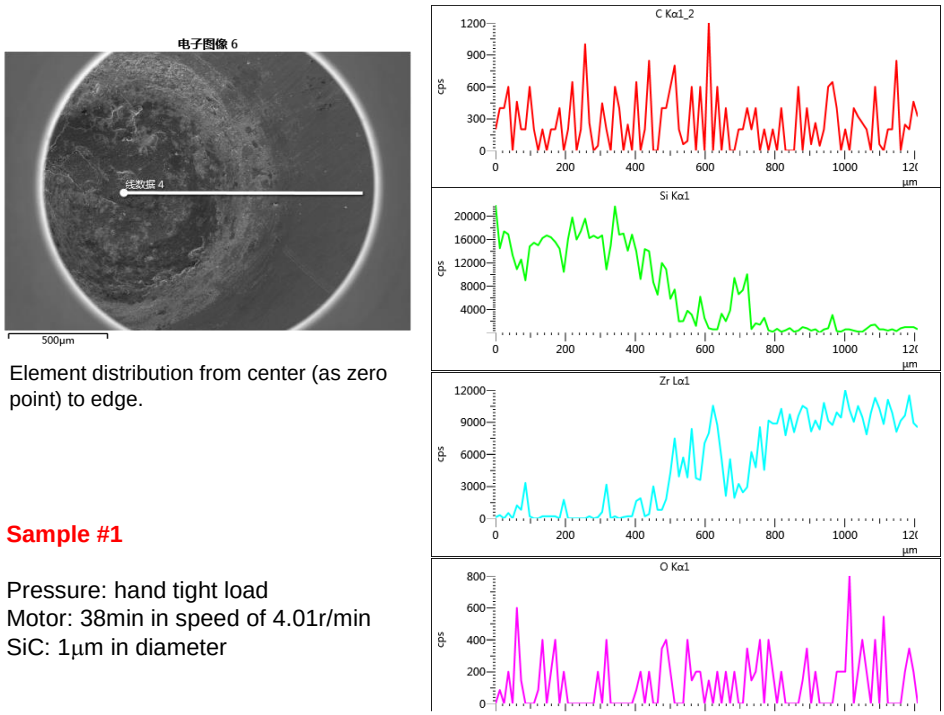

Element distribution from center (as zero point) to edge.

Sample #1

Pressure: hand tight load
Motor: 38min in speed of 4.01r/min
SiC: 1μm in diameter

Fig. 29. Element distribution from center of the sample to the edge of the gasket.

In another experiment, we recently applied shear on the sample (at similar conditions), and performed Raman scattering measurements in different regions of the sample. The measured positions are illustrated in Fig. 31.

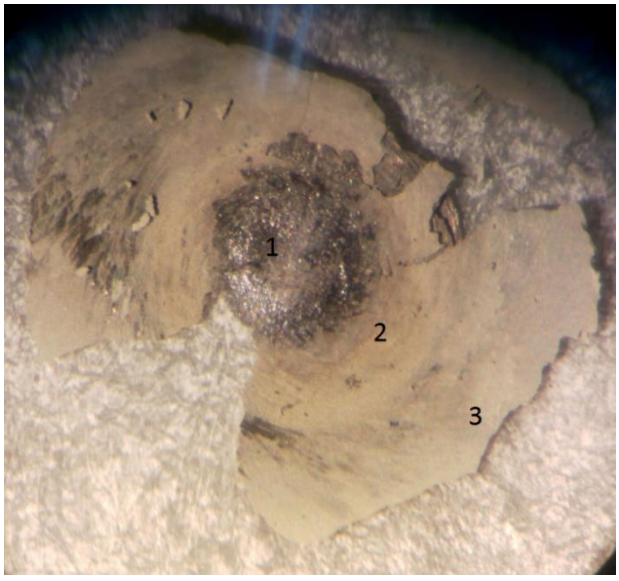

Fig. 30. The SiC sample after quenching from pressure and shear. Number 1, 2, and 3 marks the center position, the position between center and edge, and the edge position, respctively.

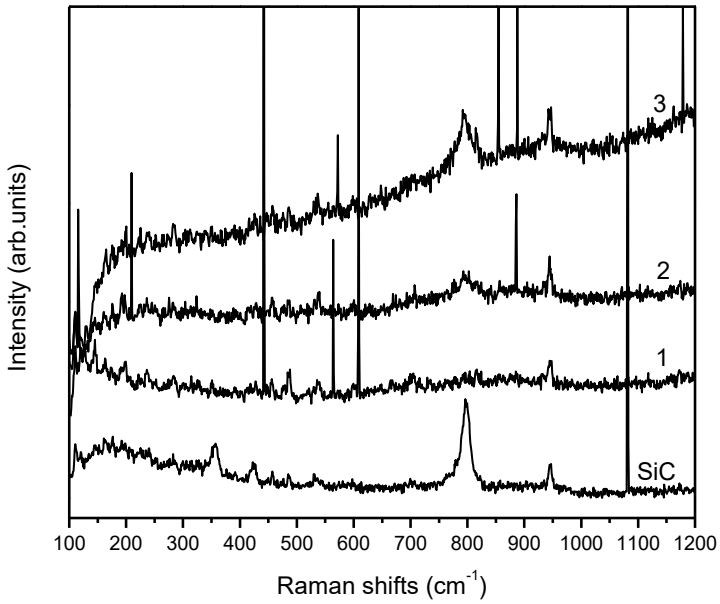

Fig. 31. The Raman spectra in the sample.

Fig. 31 gives the Raman spectra at different positions in comparison to the starting material. The spectrum shows that at the center part, the signature peak at 796 cm-1 disappears. This indicates that the shear causes a phase transition of SiC. Further analysis and experiments are underway.

2.4. New design of rotational diamond anvil cell

Jointly with the researchers from the Institute for Superhard Materials of the Ukrainian Academy of Sciences (Kiev, Ukraine), a new automated RDAC for in situ x-ray studies has been developed and manufactured [27]. The main advantage of the design is reduction of the size (and weight) by almost a factor of 2 with the same size of an anvil and accessible pressure.

In the final year (2.5-2.8):

2.5. Shear induced transition of graphite to lonsdaleite and then amorphous diamond–like phase

We applied shear on graphite at pressure up to 6.9 GPa range. We found it transforms to lonsdaleite (hexagonal diamond) and then to diamond-like amorphous.

- At 0.2 GPa or lower, at application of shear, hexagonal diamond (lonsdaleite) begins to form.
- At sufficient shear (630^o anvil rotation while pressure ramped to 6.9 GPa then drop to 3.7 GPa), the graphite phase completely disappears.
- Continuing application of shear lead to the amorphization of lonsdaleite.
- The amorphous phase is quenchable with trace of residue lonsdaleite phase.
- The quenched amorphous phase has much higher sp^3 to sp^2 bonding ratio.
- The amorphous phase is a superhard phase.

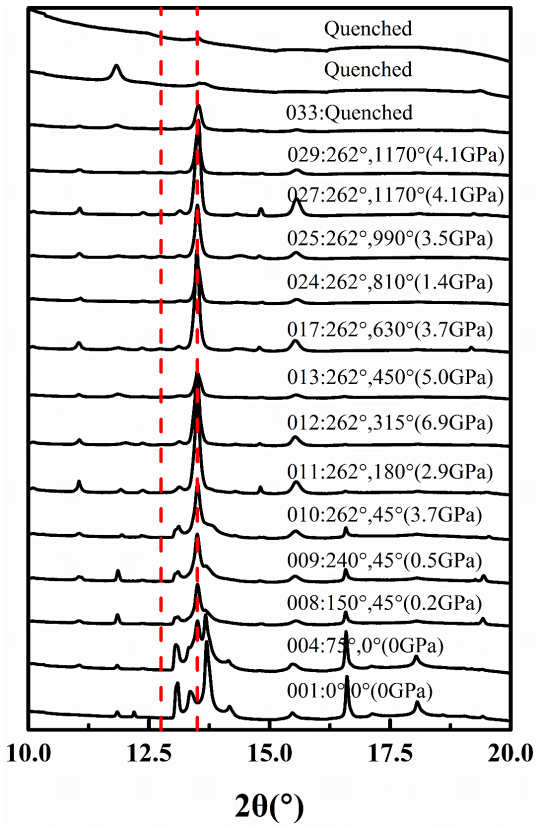

Fig. 32. Selected XRD patterns at pressure and shear operation. The numbers shown are in the order of file number, degree of applied load, and the degree of anvil rotation, and pressures calculated from gold equation of state. The (100) peak position at 2.19 Å, and the (002) peak position at 2.06 Å of lonsdaleite are marked by the red dashed lines. Both peaks grew to a full ring as shear stress and pressure was introduced in the experiment. At last, only the (002) peak was reserved when quenched from the anvil. Both peaks appeared very early in the experiment, (001) appeared at 0.2 GPa, which we claim as the transformation pressure.

2.5.1. In situ synchrotron X-ray monitoring the transition process

We used synchrotron X-ray diffraction to in situ monitor the transition progress of graphite at combined pressure and shear operations (Fig. 33). At the beginning of the experiment, the (100) diffraction peak from lonsdaleite is not observed. Similarly, at the end of the experiment, the (100) diffraction peak disappeared when sample was quenched from the cell. According to the fitting results the (100) peak of lonsdaleite first appeared at 0.2 GPa (Fig. 33). The (100) diffraction went through 4 stages. In the first stage (below 0.2 GPa with initial shear operation), the ring didn't appear. In the second stage (after 0.2 GPa and extensive shear), the ring appeared in the middle vertically, but was very week even after integration. In the third stage (completion stage) and quenched while sample inside the chamber, the diffraction ring grew to a whole ring in the pattern and the intensity after integration varied with position where the x-ray went through the sample. In the fourth stage (quenched from the anvil), the peak disappeared (Figs. 32 and 33, and table).

These phenomena indicate the initial formation of hexagonal lonsdaleite phase, its growth, completion, and the amorphization of the lonsdaleite phase.

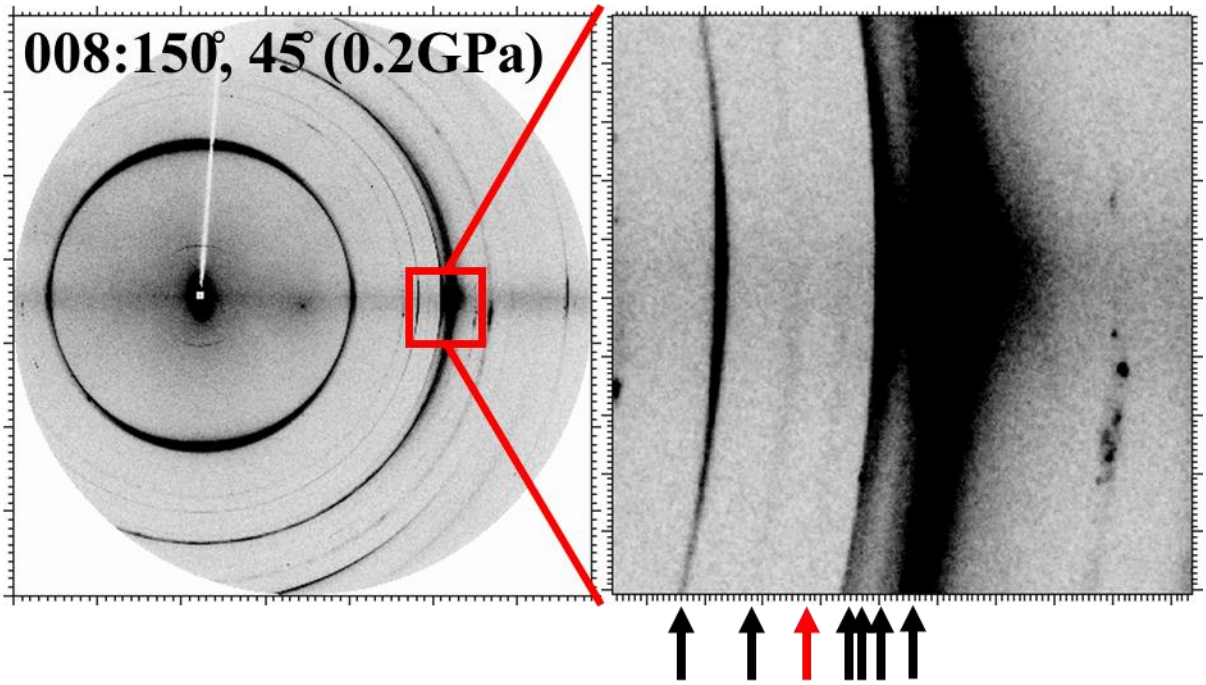

Fig. 33. The first appearance of the (100) peak at 0.219 GPa.

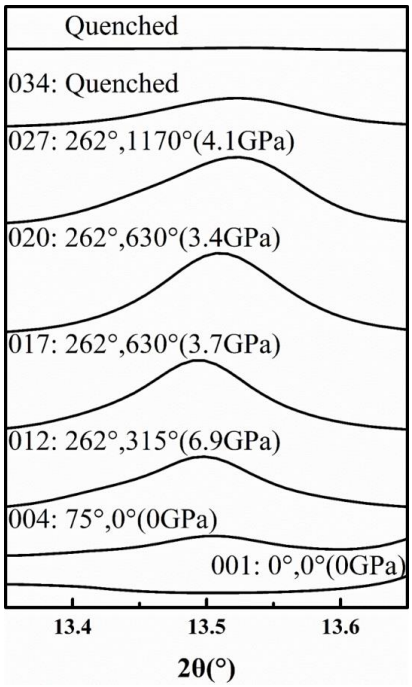

Fig. 34. The intensity change of the (002) peak of lonsdaleite phase at pressure-shear loading and unloading.

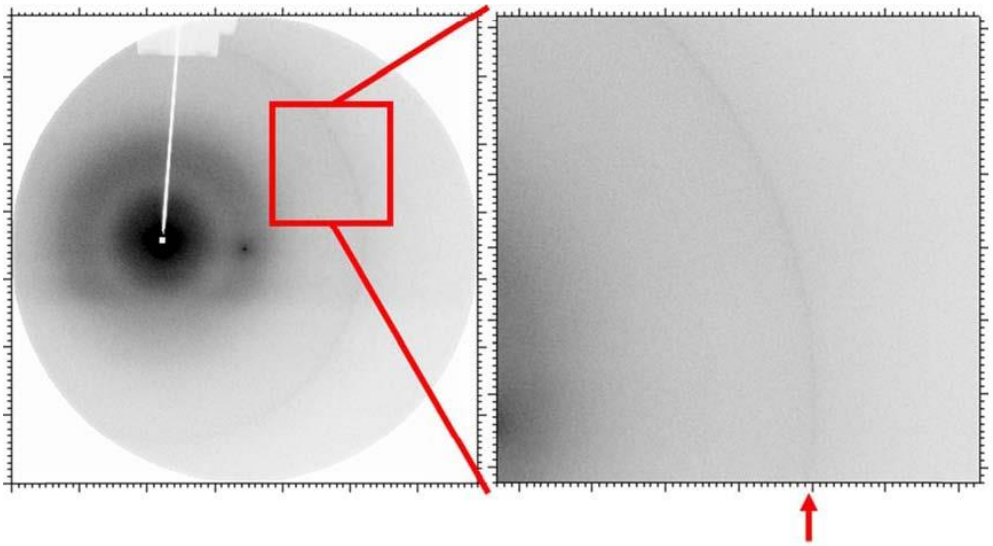

Fig. 35. The XRD pattern from the quenched sample (outside of cell— the entire sample). The weak diffraction is believed to come from the residual high pressure phase. The ring marked with the red arrow is 2.062 Å (from lonsdaleite). A broad ring ranging from 5 .9 Å to 3.9 Å is also observed in this pattern. The broad ring indicates the amorphization of graphite.

Comparison of d-spacings

Quenched sample/Å	Lonsdaleite/Å	Diamond/Å	Graphite_2H/Å	Graphite_3R/Å
2.15	2.19		2.14	
	2.06	2.06	2.039	2.08
1.96	1.92			1.96
			1.81	
			1.68	1.67
	1.5		1.55	
	1.26	1.26	1.23	1.22
				1.19
1.14	1.17		1.16	1.15
			1.12	1.11
		1.08	1.06	1.08

2.5.2 Raman measurements

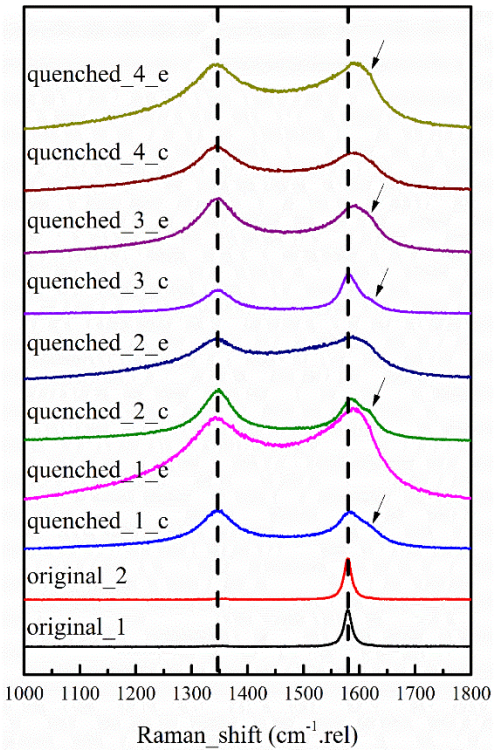

Fig. 36. Raman spectra of the quenched sample at different positions compared to the starting graphite.

As shown in Fig. 36, a G-band at ~1590 cm^{-1} and a D-band at 1350 cm^{-1} are identical to nanocrystalline diamond of sizes 5~50 μm (P.-H. Chung et. Al, Surface Science 601 (2007) 33866–387). A peak at ~1610 cm^{-1} was also observed. The peak was from the residual nanocrystalline grapphite (Andrea Carlo Ferrari and John Robertson, The Royal Society, 10.11098/rsta.2004.1452).

2.5.3 TEM measurements

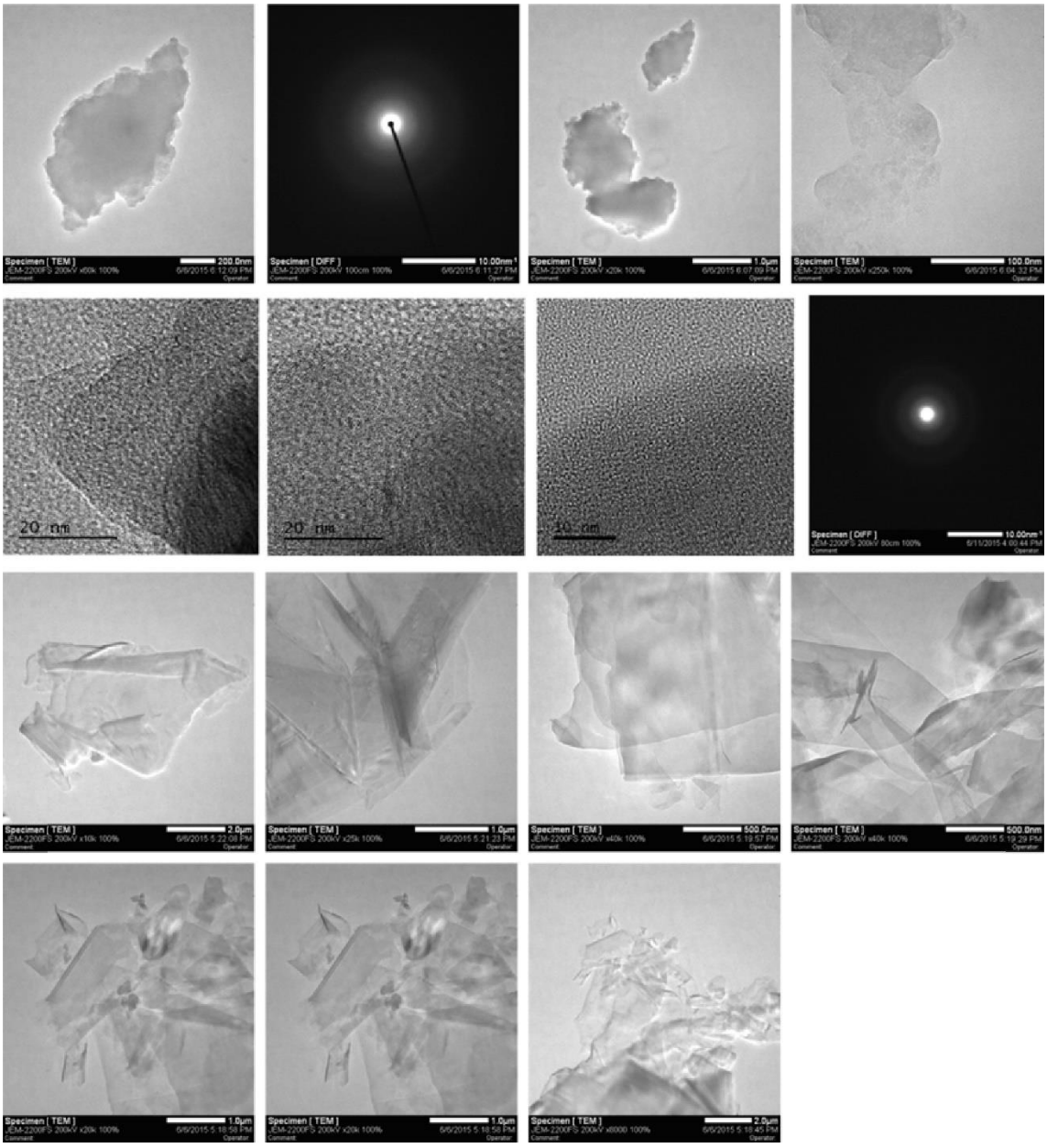

Fig 37. TEM image and electron diffraction at different level of magnification of the quenched sample compared to the o original graphite. In top two rows, the images arefrom the processed sample. In the bottom, the images are from starting graphite sample.

In the TEM image (Fig. 37), we can see that the processed sample is in the amorphous state. Yet in the diffraction at higher resolution, we did observe some texture and the broad diffraction rings at ~2.115 Å, 1.96 ÅÅ, and 1.14 ÅÅ. These can be considered as the residual hexagonal lonsdaleite phase.

In literature, under hydrostatic conditions, amorphous diamond was obtained at pressures above 33 and 40 GPa from a glassy precursor, but was not quenchable. The reversible graphite

to lonsdaleite transition was observed at 16-30 GPa under pressure; the irreversible graphite to lonsdaleite transition has been obtained at 17 and 19 GPa under shear (Blank & Estrin, 2014); at 19 GPa sample also contained cubic diamond. An almost complete transformation from graphite to cubic diamond has been obtained under shear of 0.25 radians at 21-25 GPa (Blank & Estrin, 2014).

2.5.4 XPS measurements

When we measured the XPS spectra of the quenched sample in comparison with the original graphite, we found: 1) The graphite sp^3 to sp^2 ratio is 0.265 to 1 in the original graphite sample. The sp^3 may largely ascribed to the surface, boundary, and other imperfections in the sample.

2) In the pressure and shear processed sample, the sp^3 to sp^2 ratio becomes 0.983 to 1, i.e., increase by a factor of 2.70. This mainly reflects the formation of new sp^3 bonding in the transformed amorphous phase.

3) We realized the formation of C-O bonding which is 0.579 to 1 to the sp^2 bonding. Thus pressure and shear will also lead to reaction of oxygen with carbon.

4) We tried to remove the oxygen by loading and processing the sample in nitrogen environment. We found out that the C-O bonding has been substantially but not completely reduced, which may be due to the existence of absorbed oxygen in the graphite sample.

5) Our result indicates that the amorphous phase formed after processing has significantly high percentage of sp^3 bonding, if not all.

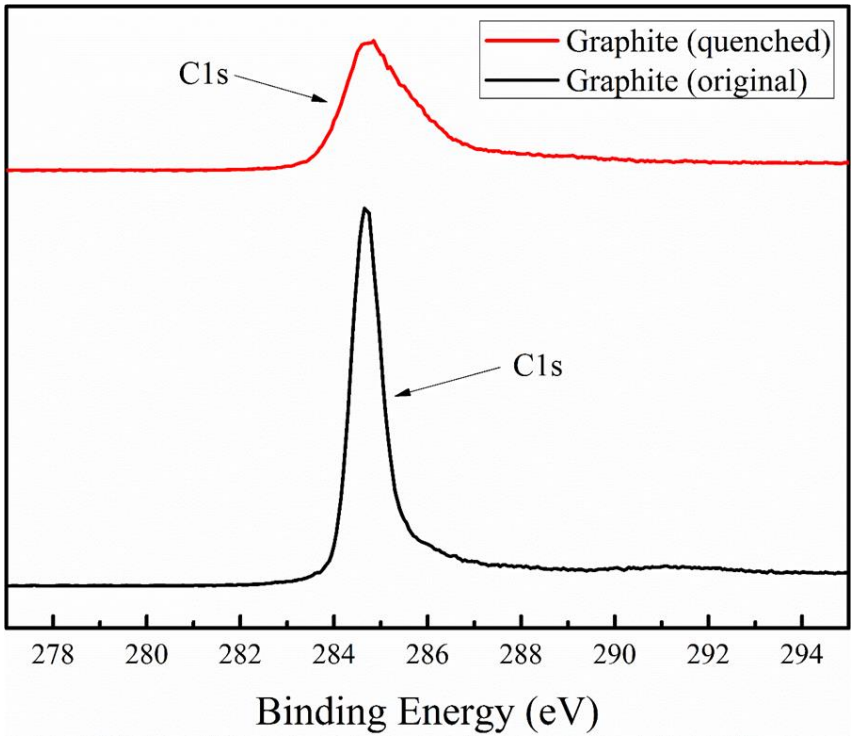

Fig. 38. Measured XPS spectra of the quenched sample in comparison with the original graphite.

XPS result of graphite under N_2 environment cont.

		Position/eV	Area	FWHM/eV		SP^3/SP^2
1	original	284.682	165395	0.7000	sp2	0.265
		285.260	43827.5	2.123	sp3	
2	nitrogen	284.574	72194.6	0.9430	sp2	1.186
quenched	3 peaks	285.039	85647.6	1.846	sp3	
	background	287.221	15869.7	1.833	C-O	
	290-276					
3	nitrogen	284.578	77821.4	1.010	sp2	0.868
quenched	3 peaks	285.058	67619.4	1.765	sp3	
	background	286.375	31320.2	4.110	C-O	
	291-276					
The difference between 2 and 3 is the background selection. The background selection doesn't influence the peak position of sp2 and sp3 that much, but influences intensity as well as the peak position and intensity of C-O peak.						

2.6 Compression and shear of lead *[37]*

For better understanding the stress and stain field in the sample chamber of a rotational diamond anvil cell, we first explored the shear effect on one of the soft most solid material, lead. By application of large plastic shear on a lead sample in a rotational diamond anvil cell, we studied the pressure self-multiplication and the stress deviation phenomena, along with the consequential effects on a phase transformation. It is indicated that pressure can be promoted by the gradual addition of shear. The stress deviation in the sample along different Chi angles is minimal and within the systematic error range. It is thus specified that a quasi-hydrostatic condition is generated in the sample chamber. Moreover, surprisingly, under such shear-controlled pressure elevation, the lead fcc-to-hcp phase transformation pressure is found to initiate and complete respectively at 12.8 and 18.5 GPa, which is identical to those observed in hydrostatic compressions. The phenomena of the so-launched quasi-hydrostatic pressure, the self-multiplication, along with the consequential effects on the phase transformation properties by shear at pressures is expected to lead to further understanding of materials as well as to potential new technologies at extremes.

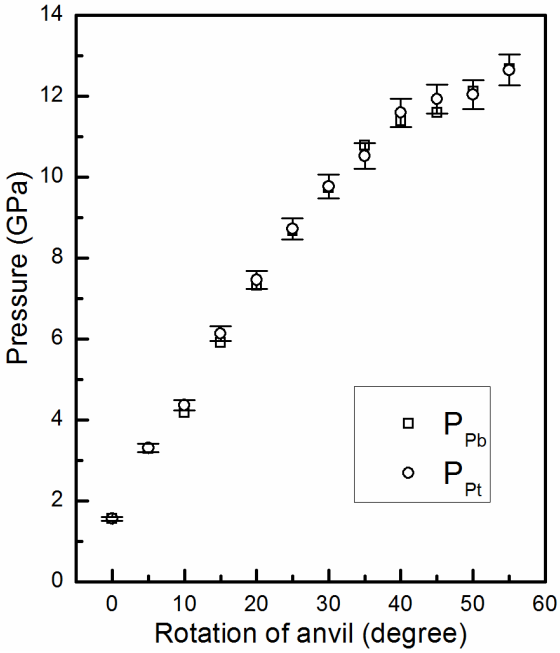

Fig. 39. Pressure in lead during anvil rotation at constant applied force. P_{Pb} and P_{Pt} are pressures calculated from EOS of Pb and Pt. Error of P_{Pt} is determined by the error of Pt's unit cell volume.

ISU group attempted to theoretically interpret the obtained at Texas Tech results. Our theory predicts that at deformation above recrystallization temperature, the effect of plastic shear should be absent because any accumulation of defects will be eliminated by recrystallization. For lead, recrystallization temperature is below room temperature. Thus, effect of shear should be negligible, which is consistent with experiments. This is conceptual confirmation of our theory. Pressure-self multiplication effect during shear without PT and at constant applied force should be caused by redistribution of stresses between sample and gasket: pressure reduces in gasket and, to keep the same force, should be increased in a sample. Large pressure gradient is expected in a Zr gasket because of relatively high yield strength. Thus, this is a system behavior rather than material behavior. The low yield strength in shear of lead (~0.01 GPa), negligible with the operating pressure of ~10 GPa, explains negligible non-hydrostaticity of stresses in experiment.

2.7 The High-Pressure Compressibility of $B_{12}P_2$ (paper under review)

Boron and boron-rich compounds are of interest for their extreme properties such as their high hardness, chemical inertness, good thermal stability, and resistance to radiation damage. These properties are a consequence of their unusual chemical bonding and the boron atoms tends to form various types of chains and clusters. Usually, the boron icosahedra are piled together in a close packed arrangement, and when other elements are present, they fit in the gaps between icosahedra. Previous Raman studies have reported that $B_{12}P_2$ experience no structural phase transition until 80 GPa before a reversible transition to a distorted structure is caused by the deformation of the icosahedral structures. Recently, An and Goodard predicted that boron suboxide (B_6O) and icosahedral boron phosphide ($B_{12}P_2$) should be much less brittle than boron

carbide due to their ability to reform bonds between planes as they slip past each other. In contrast, boron carbide does not have this ability. Thus B_6O and $B_{12}P_2$ may be superior to boron carbide in applications in which the material is subjected to high strain rates such as in armor. In situ high pressure synchrotron X-ray diffraction measurements were performed on icosahedral boron phosphide ($B_{12}P_2$) to 43.2 GPa. No structural phase transition occurs over this pressure range. The bulk modulus of $B_{12}P_2$ is $K_{OT} = 207 \pm 7\ GPa$ with pressure derivative of $K'_{OT} = 6.6 \pm 0.8$. The structure is most compressible along the chain formed by phosphorus and boron atoms in the crystal structure. The compressibility of boron-rich compounds at close to ambient pressure is determined by the boron icosahedral structure, while the inclusive atoms (both boron and non-boron between the icosahedra determine the high-pressure compressibility and structure stability.

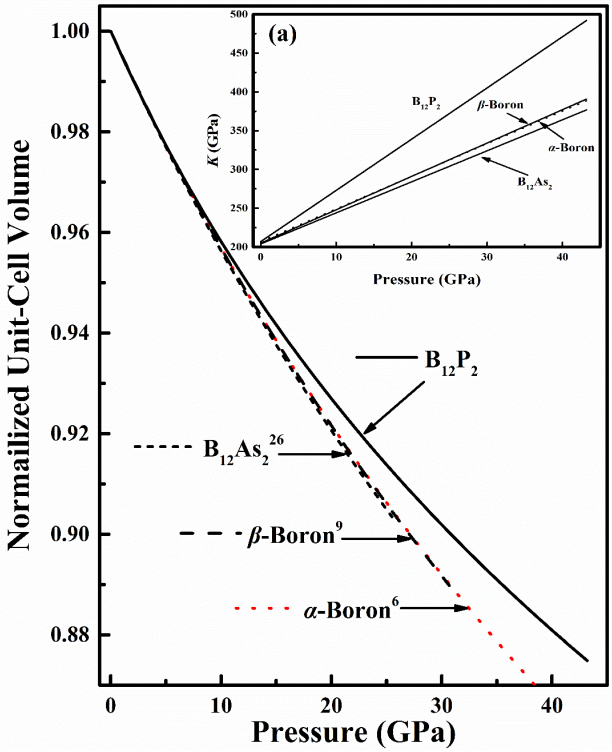

Fig. 40. Comparison of the pressure dependent unit-cell volume of $B_{12}P_2$, $B_{12}As_2$, α-and β-boron. The pressure dependence of bulk moduli for $B_{12}P_2$, $B_{12}As_2$, β-boron and α-boron is shown in inset (a).

2.8. Shear and transformation bands in the fullerene [34]. This part is collaborative efforts between ISU and V. Blank group from the Technological Institute for Superhard and Novel Carbon Materials (Moscow, Russia). The C_{60} fullerene has been investigated by TEM and electron energy loss spectroscopy after treatment of fcc phase in a RDAC. Shear transformation-deformation bands have been revealed (Fig. 4) consisting of shear-strain-induced nanocrystals of linearly-polymerized fullerene and polytypes, the triclinic, monoclinic, and hcp C_{60}, and amorphous structures. Thus, plastic straining arrests five high pressure phases under normal pressure, which may be important for their engineering applications. Localized shear deformation looks contradictory because high pressure phases of C_{60} are stronger than the initial

low pressure phase. However, this was explained by transformation-induced plasticity during localized PTs which occurs because of a combination of applied stresses and internal stresses due to a volume reduction during PTs. Localized PTs and plastic shear deformation promote each other producing positive mechanochemical feedback and cascading structural changes. Obtained results demonstrate that transformation kinetics cannot be analyzed in terms of prescribed shear and methods to measure local shear should be developed.

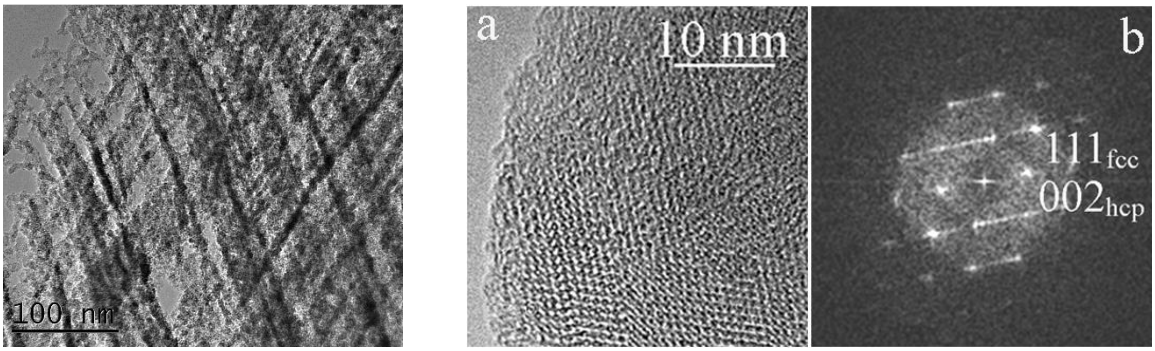

Fig. 41. Shear bands in fullerene C_{60} after pressure-shear treatment (left) and stacking faults and polytypes in C_{60} formed in a shear band (a) and the corresponding Fourier transform (b).

Journal Publications

1. Feng B., Levitas V.I., and Zarechnyy O. M. Plastic flows and phase transformations in materials under compression in diamond anvil cell: Effect of contact sliding. Journal of Applied Physics, 2013, Vol. 114, 043506, 12 pages.
2. Levitas V.I. and Javanbakht M. Phase field approach to interaction of phase transformation and dislocation evolution. Applied Physics Letters, 2013, Vol. 102, 251904.
3. Levitas V.I. Thermodynamically consistent phase field approach to phase transformations with interface stresses. Acta Materialia, 2013, Vol. 61, 4305-4319.
4. Levitas V.I. Phase-field theory for martensitic phase transformations at large strains. International Journal of Plasticity, 2013, Vol. 49, 85–118.
5. Levin V. A., Levitas V. I., Zingerman K.M., Freiman E.I. Phase-field simulation of stress-induced martensitic phase transformations at large strains. International Journal of Solids and Structures, 2013, Vol. 50, 2914-2928.
6. Levitas V.I. Interface Stresses for Nonequilibrium Microstructures in Phase Field Approach: Exact Analytical Results. Physical Review B, 2013, Vol. 87, 054112.
7. Feng B., Zarechnyy O. M., and Levitas V.I. Strain-induced phase transformations under compression, unloading, and reloading in a diamond anvil cell. Journal of Applied Physics, 2013, Vol. 113, 173514, 9 pages.
8. Ji C., Levitas V. I., Zhu H., Chaudhuri J., Marathe A., and Ma Y. Shear-Induced phase transition of nanocrystalline hexagonal boron nitride to wurtzic structure at room temperature and lower pressure. Proceedings of the National Academy of Sciences of the United States of America, 2012, Vol. 109, No. 33, 201203285.
9. Levitas V. I., and Javanbakht M. Advanced phase-field approach to dislocation evolution. Physical Review B, Rapid Communication, 2012, Vol. 86, 140101 (R).

10. Levitas V. I., and Ravelo R. Virtual melting as a new mechanism of stress relaxation under high strain rate loading. Proceedings of the National Academy of Sciences of the United States of America, 2012, Vol. 109, No. 33, 13204-13207.

    Featured in: P. Ball. Shock relief. Nature Materials, 2012, Vol. 11, p. 747 ; S.M. Dambrot. Crystals take a chill pill: A thermomechanical theory of low-temperature melting. August 21, 2012 http://phys.org/news/2012-08-crystals-chill-pill-thermomechanical-theory.html.
11. Feng B., and Levitas V. I. Coupled phase transformations and plastic flows under torsion at high pressure in rotational diamond anvil cell: Effect of contact sliding. Journal of Applied Physics, 2013, Vol. 114, No. 21, 213514, 12 pages.
12. Levitas V. I., Roy A. M., and Preston D. L. Multiple twinning and variant-variant transformations in martensite: phase-field approach. Physical Review B, 2013, Vol. 88, 054113, 8 pages.
13. Feng B., Levitas V.I., and Zarechnyy O. Strain-induced phase transformations under high pressure and large shear in a rotational diamond anvil cell: Simulation of loading, unloading, and reloading. Computational Materials Science, 2014, Vol. 84, 404-416.
14. Feng B., Levitas V. I., and Ma Y. Strain-induced phase transformation under compression in a diamond anvil cell: simulations of a sample and gasket. Journal of Applied Physics, 2014, Vol. 115, No. 16, 163509, 14 pages.
15. Levitas V. I. Unambiguous Gibbs dividing surface for nonequilibrium finite-width interface: Static equivalence approach. Physical Review B, 2014, Vol. 89, 094107, 5 pages.
16. Levitas V. I., and Javanbakht M. Phase transformations in nanograin materials under high pressure and plastic shear: nanoscale mechanisms. Nanoscale, 2014, Vol. 6, No. 1, 162-166.
17. Levitas V. I., and Momeni K. Solid-solid transformations via nanoscale intermediate interfacial phase: multiple structure, scale and mechanics effects. Acta Materialia, 2014, Vol. 65, 125-132.
18. Momeni K., and Levitas V. I. Propagating phase interface with intermediate interfacial phase: phase field approach. Physical Review B, 2014, Vol. 89, 184102, 24 pages.
19. Levitas V. I. Phase field approach to martensitic phase transformations with large strains and interface stresses, Journal of the Mechanics and Physics of Solids, 2014, Vol. 70, 154–189.
20. Levitas V.I. and Javanbakht M. Thermodynamically consistent phase field approach to dislocation evolution at small and large strains. Journal of the Mechanics and Physics of Solids, 2015, 82, 345-366.
21. Momeni K. and Levitas V.I. A Phase-Field Approach to Solid-Solid Phase Transformations via Intermediate Interfacial Phases under Stress Tensor. International Journal of Solids and Structures, 2015, Vol. 71, 39-56.
22. Levitas V.I. and Javanbakht M. Interaction between phase transformations and dislocations at the nanoscale. Part 1. General phase field approach. Journal of the Mechanics and Physics of Solids, 2015, Vol. 82, 287-319.
23. Javanbakht M. and Levitas V.I. Interaction between phase transformations and dislocations at the nanoscale. Part 2. Phase field simulation examples. Journal of the Mechanics and Physics of Solids, 2015, Vol. 82, 164-185.

24. Levitas V.I. and Roy A.M. Multiphase phase field theory for temperature- and stress-induced phase transformations. Physical Review B, 2015, Vol. 91, No.17, 174109.
25. Momeni K., Levitas V.I., and Warren J.A. The strong influence of internal stresses on the nucleation of a nanosized, deeply undercooled melt at a solid-solid interface. Nano Letters, 2015, Vol. 15, No. 4, 2298-2303.
26. Levitas V.I. and Javanbakht M. Interaction of phase transformations and plasticity at the nanoscale: phase field approach. Materials Today, 2015, Vol. 2S, S493-S498.
27. Novikov N.V., Shvedov L.K., Krivosheya Yu. N., Levitas, V.I. New Automated Shear Cell with Diamond Anvils for in situ Studies of Materials Using X-ray Diffraction. Journal of Superhard Materials, 2015, Vol. 37, No. 1, 1-7.
28. Levitas V.I. and Warren J.A. Thermodynamically consistent phase field theory of phase transformations with anisotropic interface energies and stresses. Physical Review B, 2015, Vol. 92, 144106, 16 pages.
29. Momeni K. and Levitas V.I. A phase-field approach to nonequilibrium phase transformations in elastic solids via an intermediate phase (melt) allowing for interface stresses. Physical Chemistry Chemical Physics, 2016, Vol. 18, 12183-12203.
30. Feng B. Levitas V. I., and Hemley R.J. Large elastoplasticity under static megabar pressures: Formulation and application to compression of samples in diamond anvil cells. International Journal of Plasticity, 2016, (In press), doi:10.1016/j.ijplas.2016.04.017.
31. Feng B. and Levitas V. I. Effects of gasket on coupled plastic flow and strain-induced phase transformations under high pressure and large torsion in a rotational diamond anvil cell. Journal of Applied Physics, 2016, Vol. 119, 015902, 12 pages.
32. Levitas V.I. and Warren J.A. Phase field approach with anisotropic interface energy and interface stresses: Large strain formulation. Journal of the Mechanics and Physics of Solids, 2016, Vol. 91, 94-125.
33. Levitas, V.I., Ren, Z., Zeng, Y., Zhang, Z.,Han, G. Crystal-crystal phase transformation via surface-induced virtual pre-melting. Phys. Rev. B 85, 220104, 2012.
34. Kulnitskiy B.A., Blank V.D., Levitas V.I., Perezhogin I.A., Popov M.Y., Kirichenko A.N., and Tyukalova E.V. Transformation-deformation bands in C_{60} after the treatment in a shear diamond anvil cell. Materials Research Express, 2016, Vol. 3, 045601, 7 pages.
35. Javanbakht M. and Levitas V.I. Phase field approach to dislocation evolution at large strains: computational aspects. International Journal of Solids and Structures, 2016, Vol. 82, 95-110.
36. Levitas V. I. and Roy A. M. Multiphase phase field theory for temperature-induced phase transformations: Formulation and application to interfacial phases. Acta Materialia, 2016, Vol. 105, 244-257.
37. Wang H., Cui Q., Liu B., Gao Y., Li Z., Ma Y. Compression and shear on lead in a rotational diamond anvil cell. High Pressure Research, 2016, Vol. 36, 55-62.

This work was leveraged by the support from DARPA, NSF, ONR, and PI's endowment.